RESEARCH ARTICLE - SOLID EARTH SCIENCES

The 2021–2022 Mw 6.0 Bejaia Bay, NE Algeria, earthquake sequence: tectonic implications at the Algerian margin between lesser and greater Kabylian blocks

Abdelkarim Yelles-Chaouche[1] · Issam Abacha[1] · Oualid Boulahia[1] · Hamoud Beldjoudi[1] · Chafik Aidi[1] · Hichem Bendjama[1] · El-Mahdi Tikhamarine[2] · Yahia Mohammedi[1] · Adel Chami[1] · Redouane Chimouni[1] · Abdelaziz Kherroubi[1]

Abstract

On March 18, 2021, at 00:04 UTC, a strong earthquake (Mw 6.0) hit Bejaia city, 200 km east of Algiers. Its epicenter was 15 km northeast of Cap Carbon in Bejaia Bay, making it the largest earthquake recorded offshore since the devastating earthquake (Mw 6.8) in Boumerdes on May 21, 2003. The earthquake had a maximum intensity of VII (EMS 98), triggering hundreds of aftershocks and damaging 2000 houses and social infrastructures, as well as causing several rock falls along the rocky coastline, but no human casualties were reported. The waveform inversion and spectral analysis of the mainshock and its largest aftershocks indicate an alignment along an E-W thrust fault plane offshore, dipping southward, the mainshock seismic moment of $M_0 = 9.7e + 17$ N.m. corresponding to a magnitude Mw = 6.0. The aftershocks illuminated a surface 22 km long (N–S) and 12 km wide; their statistical parameters were assessed by Guttenberg–Richter relationship, Omori decay, and temporal clustering. The b-value is estimated at 0.83, the p value at 0.95, and the n-value at 0.75 (i.e., 75% triggered events), which follows classical patterns of aftershock sequences and suggests the sequence tectonic genesis. Furthermore, previous studies showed that the epicentral area was positively charged by coseismic static stresses transferred from recent events in the Bejaia–Jijel margin. Exactly one year later, on March 19, 2022, a moderate earthquake struck the same epicentral zone, 3 km NW of the first shock, generating a moment $M_0 = 8.5e + 16$ N.m. corresponding to a magnitude Mw = 5.3; its focal mechanism also revealed an E–W striking reverse fault with a small strike-slip component. The present-day local stress field is characterized by a contractional tectonic regime ($R' = 2.99 \pm 0.24$) and σ1 orientation (N345°E) consistent with the maximum regional compressive stress direction (NNW–SSE). The 2021–2022 Bejaia Bay seismic sequence underlined the active tectonics linking the major E–W offshore thrust fault system and the NW–SE strike-slip Babors Transverse Fault system. This sequence, along with a number of other earthquakes that occurred around the Lesser Kabylia Block (LKB) over the last decade, likely highlights the ongoing incipient subduction process between Africa and Eurasia along the northern Algerian margin.

Keywords Bejaia Bay earthquake · Algerian margin · Waveform modeling · Source parameters · Thrust fault · Incipient subduction

✉ Issam Abacha
abacha.issam@yahoo.fr

1 Research Center in Astronomy, Astrophysics, and Geophysics, 16340 Algiers, Algeria

2 University Ferhat Abbas of Setif, Setif, Algeria
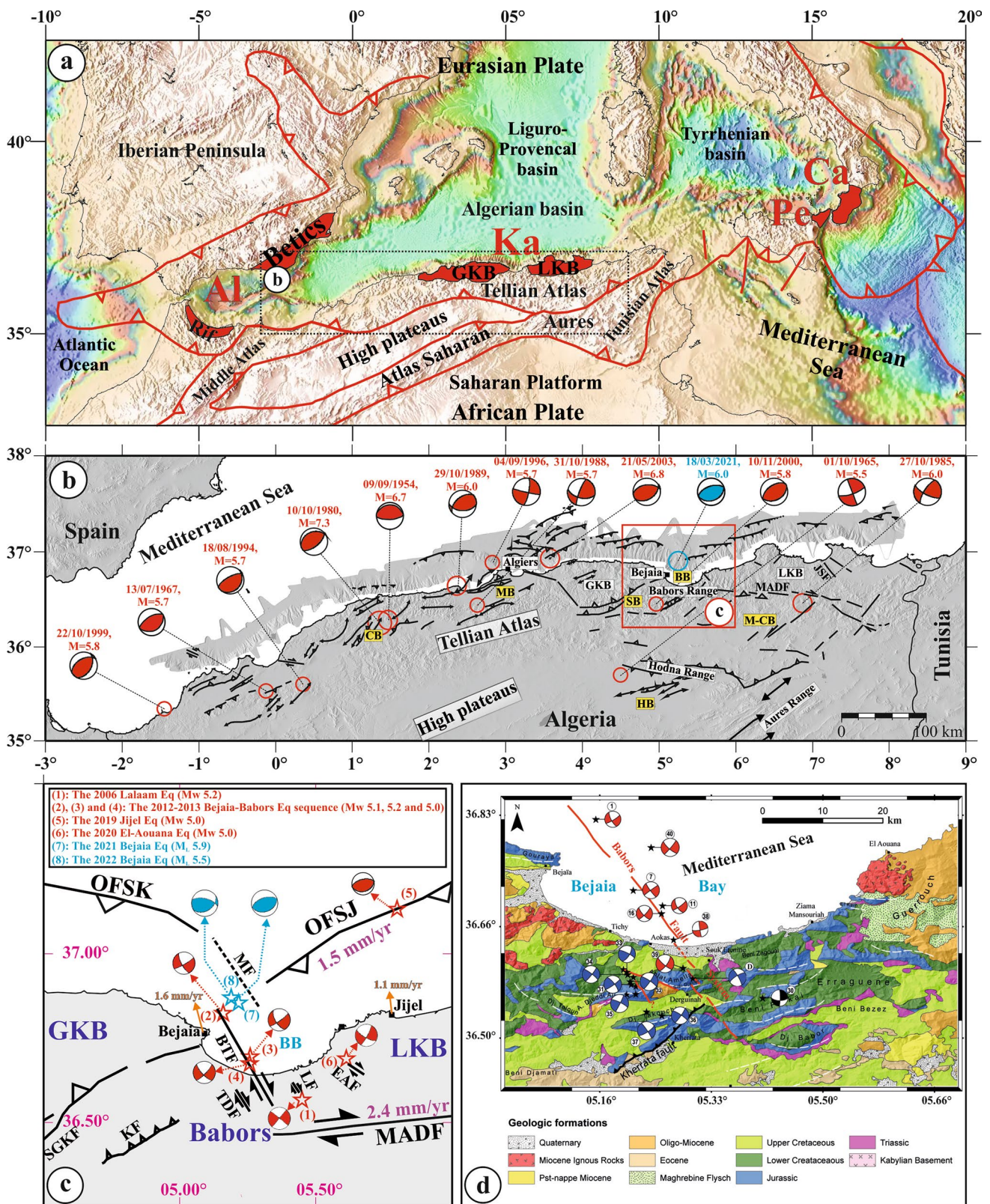
Introduction

In the last decade, there has been intense seismic activity in eastern Algeria around the Lesser Kabylian Block (LKB) (Yelles-Chaouche et al. 2022), one of the two main blocks representing the internal domain of the Maghrebides Chain (Fig. 1a). The active structures fringing the LKB are: The E-W Offshore Thrust Fault System (OFS) in the north, the NW–SE Babors Transverse Fault (BTF) system in the west, the major E–W Mcid Aïcha-Debbagh (MAD) fault in the

south, and the NE–SW Jebel Safia Fault (JSF) in the east (Abacha et al. 2023) (Fig. 1b). The strain resulting from Africa–Eurasia convergence is distributed among the tectonic structures bordering the LKB, giving rise to mainshocks that predominantly occur with magnitudes either greater or lesser than 5.

◀**Fig. 1 a** Geological map of the Western Mediterranean highlighting the main geological units. The red areas correspond to the AlKaPeCa fragments, including the Alboran Basin (AL), Kabylides (Ka) represented by the Greater and Lesser Kabylia Blocks (GKB and LKB), Peloritani Mountains (Pe), and Calabria Terrane (C). The Maghrebides Chain encompasses the Tellian Atlas and Rif. **b** Seismotectonic map of northern Algeria displaying the major active faults observed in the Tellian Atlas, based on Abacha (2015) and related references. Additionally, large earthquakes (M ≥ 5.5) and their focal mechanisms are depicted. The Neogene seismogenic basins, namely Cheliff basin (CB), Mitidja basin (MC), Mila-Constantine basin (M-CB), Soummam basin (SB), Hodna basin (HB), and Bejaia Bay (BB), are indicated within yellow rectangles. **c** Distribution of epicenters for the March 18, 2021, and March 19, 2022, Bejaia Bay mainshocks (in blue), along with other significant recent events (in red) and principal active faults (OFSJ = Offshore Fault System of Jijel, OFSK = Offshore Fault System of Kabylia, BTF = Babors Transverse Fault, TDF = Tizi N'Berber-Darguinah Fault, LF = Lalaam Fault, MF = Maradja Fault, and EAF = El Aouana Fault). **d** Geological map illustrating the main stratigraphic units in the Babors chain, sourced from Boulahia et al. (2021)

Off LKB, the July 13, 2019, Jijel earthquake Mw 5.0 (Yelles-Chaouche et al. 2021) was the strongest event located near Jijel's city after the tsunamigenic and destructive earthquake (I_0:10) on August 21–22, 1856. Therefore, precious indicators were provided to better understand the rupture process of a previously identified set of three ~E–W en echelon faults along the Jijel margin (Yelles-Chaouche et al. 2009). In western LKB, the 2012–2013 Bejaia earthquake sequence, with three mainshocks of magnitude $5.0 \leq Mw \leq 5.2$, identified the NW–SE strike-slip Babors Transverse Fault system (Boulahia et al. 2021). In addition, the January 24, 2020, El Aouana earthquake of Mw 5.0, near Jijel city, the recent seismic activity (2012–2021) in and around the El Aouana area together with pre-existing geological observations, led to the suggestion of a new NW−SE right-lateral shear zone between LKB and GKB (Abacha et al. 2023). In southern LKB, the July 17 and August 8, 2020, Mila earthquakes of Mw 4.8 and 5.0, respectively, the November 22, 2020, El Kantour earthquake of Mw 5.3, and the April 1, 2021, Guelma earthquake of Mw 5.0, gave insights into fault segment geometry and their rupture process along the major E-W strike-slip MAD fault (Bendjama 2022). Alternatively, several marine projects, including MARADJA1 in 2003, MARADJA2 in 2005 (Yelles-Chaouche and the Maradja Team 2006), and SPIRAL in 2009 (Yelles-Chaouche and the Spiral Team 2010), studied the structure of the margin, characterized the deformation pattern, and imaged the deep structure from the Algerian basin to the continent, providing fruitful information on the continuous inversion process that has affected the Algerian margin since the Pliocene.

The convergence of the Africa–Eurasia plates has led to ongoing deformation and seismic activity, which has raised questions about the existence of an incipient subduction process occurring along this margin. Several recent studies have suggested that the Algerian margin may indeed be undergoing an incipient subduction process (Hamai et al. 2015; 2018; Leffondré et al. 2021). Understanding the potential incipient subduction process along the Algerian margin is critical for improving our understanding of plate tectonics and the evolution of the Earth's crust, as well as for developing strategies to mitigate the potential hazards associated with the seismic activity in the region. Seismic sequence analysis is a powerful tool for gaining insights into the early stages of subduction (Wada and Wang 2009). This can provide detailed information about the temporal and spatial patterns of seismicity in these regions (Duarte et al. 2013). The new earthquake sequences in Bejaia Bay on March 18, 2021, with a magnitude M_L of 5.9 (CRAAG, Centre de Recherche en Astronomie, Astrophysique, et Géophysique), the largest earthquake recorded offshore since the devastating earthquake, Mw 6.8, in Boumerdes on May 21, 2003 (Yelles et al. 2004), and a year later, (M_L 5.5, CRAAG), on March 19, 2022, constitute an opportunity to provide new elements to the ongoing debate.

We focus on the mainshocks and aftershock sequence following the March 18, 2021, earthquake, M_L 5.9, in Bejaia Bay. By studying this sequence in detail, we aim to identify the fault geometry, driving process, and ongoing geodynamical implications. We will isolate the mainshock source parameters using waveform modeling and spectral analysis. Through accurate relocation and the spatiotemporal behavior of aftershocks, we will outline the driving process. In light of our knowledge of the active deformation along the Bejaia–Jijel margin and employing the present findings, we will discuss the ongoing deformation process.

Seismotectonic setting

The Babors mountain range, one of the main massifs of the Tellian chain, forms the southern limit of Bejaia Bay, which is the offshore part of Bejaia city. This bay is located in a complex area between two major units, the great and lesser Kabylian blocks, which constitute the internal zone of the Maghrebides chain (Fig. 1a). These metamorphic blocks are issued from the Cenozoic geodynamical evolution of the western Mediterranean region, marked by the detachment of the Alboran, Kabylie, Peloritan, and Calabria (AlKaPeCa) domains from the European margin (Bouillin 1986) (Fig. 1a), the opening of the Algerian back-arc basin (Van Hinsbergen et al. 2014), the rolling-back of the Tethysian slab (Spakman and Wortel 2004), and the suturing between the AlKaPeKa blocks and the African platform around 16.5 Myr (Schettino and Turco 2006). Nowadays, the Algerian margin deformation results generally from the oblique convergence of the African and European major plates since

the Cenozoic and particularly from an inversion process since the Pliocene (Strezynski et al. 2010). This margin is subjected to ongoing compression and is characterized by prominent seismic activity; furthermore, in its eastern part, an incipient subduction zone is suggested by several studies (Hamai 2015; 2018; Leffondré et al. 2021). Therefore, the crust displays numerous faults inherited from the Alpine orogenies and from the ongoing deformation in the Pliocene.

The active deformation in Algeria is expressed through its level of seismicity, which is distributed as follows from north to south (Yelles-Chaouche et al. 2021; 2022; Boulahia et al. 2021): (1) Along the Algerian margin, where exhaustive bathymetric mapping and seismic reflection acquisition revealed a series of crustal-scale reverse faults that emerge at the toe of the Algerian continental margin (Domzig 2006), these faults have been responsible for the high level of seismicity, including the Boumerdes earthquake of May 21, 2003, which had a magnitude of Mw 6.8 and caused significant damage and loss of life; (2) Along the Tell Atlas, which is a fold-and-thrust belt that runs E–W. The neotectonic features correspond to en echelon thrust folds and conjugate strike-slip faults, dominated by NW–SE to E–W right-lateral strike-slip faults and NE–SW left-lateral range-front thrust faults that cut the Tell (Fig. 1b). Neogene post-nappes basins, which correspond to E–W-elongated intermountain structures such as the Cheliff, Mitidja, Soummam, Hodna, and Mila-Constantine intermountain sedimentary basins, represent the main structural features in the Tell Atlas concentrating a high level of seismicity, the NE–SW-trending and right-stepped en echelon active folding of the Cheliff Basin, and the associated El Asnam active fault were responsible for the October 10, 1980, large earthquake (Mw 7.3) (Meghraoui et al. 1986); (3) Between the Tell and South-Atlas fronts, along the High plateaus and Saharan Atlas (Fig. 1a). Algeria's Atlas system (Saharan Atlas + Aures Mountains + High Plateaus) has been inverted and uplifted as a result of two major tectonic episodes. The first occurred between the Middle Eocene and the Aquitanian, causing significant deformation and the formation of large NE–SW trending folds. The second event generated E–W-trending folds and thrusts during the Pleistocene. Between these two compressive pulses, the Miocene was a period of relative quiescence, during which normal faulting developed in some places (Benaouali-Mebarek et al. 2006 and references therein). The seismic activity in this region is generally lower than the previous ones, but it is still considered to be seismically active. For example, the Gafsa region that covers the Aures Mountains and the south Atlas limit with the Sahara platform in Algeria and Tunisia shows active folding and faulting and NNW-SSE-trending active graben structures. Moderate earthquakes have affected this area (Megrahoui and Pondreli 2012). Recently, in 2016, in Biskra, along the south Atlas, an Mw 5.2 earthquake with

normal faulting occurred (Yelles-Chaouche et al. 2022). We should also note that there is a difference in seismicity distribution from west to east: In western Algeria, seismicity is confined to a narrow stripe within ~ 100 km of the coastline that coincides with the Tell Atlas. While in eastern Algeria, seismicity is more broadly distributed, stretching from the coastline to the southern confines of the Saharan Atlas (Abacha 2015; Bougrine et al. 2019).

A closer look into the Bejaia–Babors area reveals that active faulting indicates mainly four fault systems in and around the epicentral area of the studied earthquake: (1) Off LKB (The abbreviation for the Offshore Fault System of Jijel is OFSJ, as shown in Fig. 1c), based on the data collected during the Maradja 2 survey conducted in 2005 over the Algerian margin (Domzig 2006), the deformation style shows relatively discrete folds in the topography, controlled by active en echelon faults at the foot of the slop, with a WSW–SNE orientation. Yelles-Chaouche et al. (2009) modeled the historical Djidjelli earthquake on August 21–22, 1856 (I_0:X) and its associated tsunami by simulating a simultaneous rupture on a set of three en echelon faults. (2) Off GKB (The abbreviation for the Offshore Fault System of Kabylia is OFSK, as shown in Fig. 1c.), the Maradja 2 survey as well imaged the seafloor structures from Bejaia to Dellys (Domzig 2006); this margin part represents the transition between the very deep western part of the Algerian basin and the more progressively thinned eastern continental part (Aidi et al. 2018 and references therein). The Plio-Quaternary inversion of the margin is expressed as south-dipping blind thrusts under the margin emerging at the slop toe (Domzig 2006; Yelles-Chaouche et al. 2009). It roughly follows the boundary of the Greater Kabylia massif, passing from east to west in an NW–SE, E–W, and NE–SW direction. (3) the area separating LKB and GKB, based on the analysis of several moderate earthquakes between 2012 and 2020 along with previous studies, Boulahia et al. (2021) identified a new NW–SE transverse fault system that extends from Bejaia to Babors and includes several en echelon NW–SE-trending right-stepping strike-slip fault segments: the BTF, TDF (Tizi N'Berber-Darguinah Fault), LF (Lalaam Fault), and MF (Maradja Fault) (Fig. 1c). Additional data were allowed to delineate a 30–35 km wide NW-trending shear zone, bounded to the east by LKB and to the west by GKB (Abacha et al. 2023). This strike-slip corridor links the offshore thrust faults to the E–W right-lateral strike-slip Mcid Aïcha-Debbagh Fault (MADF; Fig. 1c). (4) The thrust system delineating the GKB southern boundary (Southern Greater Kabylia Faults = SGKF in Fig. 1c) where the Kabylian units thrust the Neogene sedimentary cover of the Bouira-Soummam valley (Boudiaf 1996).

At the scale of the LKB and GKB, the spatial partitioning of oblique convergence (~ 5 mm/yr) is evident through various measurements. Continuous GPS measurements

(Bougrine et al. 2019) and slip vectors derived from focal mechanisms (Abacha et al. 2023) indicate the partitioning. Around the LKB, the convergence is divided into orthogonal slip, with thrusting motion of 1.5 mm/yr, and dextral strike-slip, with shearing motion of 2.4 mm/yr. In contrast, within the GKB, thrust slip vectors align parallel to the overall NW−SE Eurasia-Africa motion, implying no partitioning. In this case, all convergence is accommodated by shortening along parallel faults and thrust folds, such as the offshore GKB and those bounding the Soummam valley. The transition from partitioning (LKB) to no partitioning (GKB) along this zone of strike-slip motion necessitates the presence of a NW−SE transverse fault system that connects the offshore fault system in the north to the MADF master fault in the south. The abrupt transition between the two blocks is manifested by a clockwise rotation of the compressive stress from NNW–SSE to N–S to accommodate the convergence. Therefore, the NW–SE transverse fault system accommodates the deformation and transmits it to the MAD fault.

Data acquisition and analysis methods

We employ an extensive network, comprising all stations of the Algerian Digital Seismological Network (hereafter ADSN) deployed across the Algerian territory, along with regular contributions from two additional stations located in Spain (Fig. 2a), to gather seismic data for the analysis of two significant events: The March 18, 2021, M_L 5.9 mainshock (referred to as MS-2021) and a second mainshock, M_L 5.5, that occurred one year later on March 19, 2022 (referred to as MS-2022). Apart from one station, CDFR, located ~ 70 km SE from the epicenter, most stations are located a few tens of kilometers away from the aftershock area. In order to improve (1) the detection capability and (2) the accuracy of the analysis, eight three-component short-period stations, with continuous recordings, were deployed a few hours after the MS-2021. These eight stations—seven SARA SS-1 and one L22 Cube sensor—were coupled to SARA SL-06 24-bit and one Omnirecs CUBE3 24-bit digitizers and installed along the shoreline of Bejaia Bay (Fig. 2b). This network was running for 45 days, since March 18 until May 01, 2021.

We manually picked the first P-wave and S-wave arrivals to locate the events and the end-time of coda signals to compute the duration magnitude M_D using the SEISAN set of programs (Havskov and Ottemoller 1999). The calculation of M_D is particularly relevant as it enables the generation of a homogeneous catalog suitable for statistical analysis, considering that Mw is computed only for significant events. To determine the absolute locations of the seismic events, we used Hypoinverse 2000 (Klein 2002). However, it is worth noting that one of the primary sources of locating residuals is the velocity model. In order to mitigate this, we established a "minimum 1D" velocity model specifically for the Bejaia–Jijel area. This was achieved through the application of the VELEST procedure (Kissling et al. 1994). We carefully select for the operation a subset of high-quality events from the hypoinverse output; root mean square (RMS) residuals ≤ 0.3, epicentral horizontal residuals (ERH) ≤ 3 km, epicentral vertical residuals (ERZ) ≤ 3 km, and a minimum of six (06) P-wave observations for each event. Since this approach required to improve iteratively the existing velocity model, we used the SPIRAL project profile that passes 50 km east of Bejaia as an a priori model (Mihoubi et al. 2014). To increase the robustness of the inversion results, a total of 200 different starting models (Fig. 2c) were generated for the inversion process. This was achieved by perturbing the selected a priori model with Gaussian noise. Subsequently, the VELEST algorithm was executed 200 times, each time using a different starting model. The final selection of the 1-D P-wave velocity model was based on its ability to minimize locating errors compared to the two trial local velocity models, namely the Bejaia–Babors area (Boulahia et al. 2021) and the El Aouana area (Abacha et al. 2023). Among the various tested models, this particular velocity model consisted of four distinct layers with P-wave velocities ranging from 5.5 to 7.1 km/s, covering depths from 0 to 20 km (Fig. 2d). The Vp/Vs ratio was calculated using the Wadati method (Chatelain 1978), resulting in a value of 1.76 (Fig. 2e). The seismic sequence was re-located using the newly developed velocity model and Vp/Vs ratio. To ensure the reliability and robustness of the dataset, a careful sorting process was applied. Events with RMS values less than 0.3 s and residual values (ERH & ERZ) less than 3 km were retained, forming a robust subset for further analysis. Finally, the relative locations of the resulting cluster were refined using the HypoDD double-difference algorithm (Waldhauser and Ellsworth 2000), which utilizes a catalog of P&S arrivals. The uncertainties associated with the relocation process were estimated using a bootstrap resampling method (Efron 1982). It is worth noting that the errors derived from the LSQR method employed in the HypoDD relocation are not reliable and have no physical meaning (e.g., Waldhauser 2001; Mesimeri 2018).

The focal mechanisms were calculated for significant events using the SPHERA program (Rivera and Cisternas 1990), incorporating at least 10 distinct P-wave polarities, which were identified during the arrival picking process. We also employed the waveform modeling technique developed by Yagi and Nichimura (2011) to independently calculate the seismic scalar moments (M_0), moment magnitudes
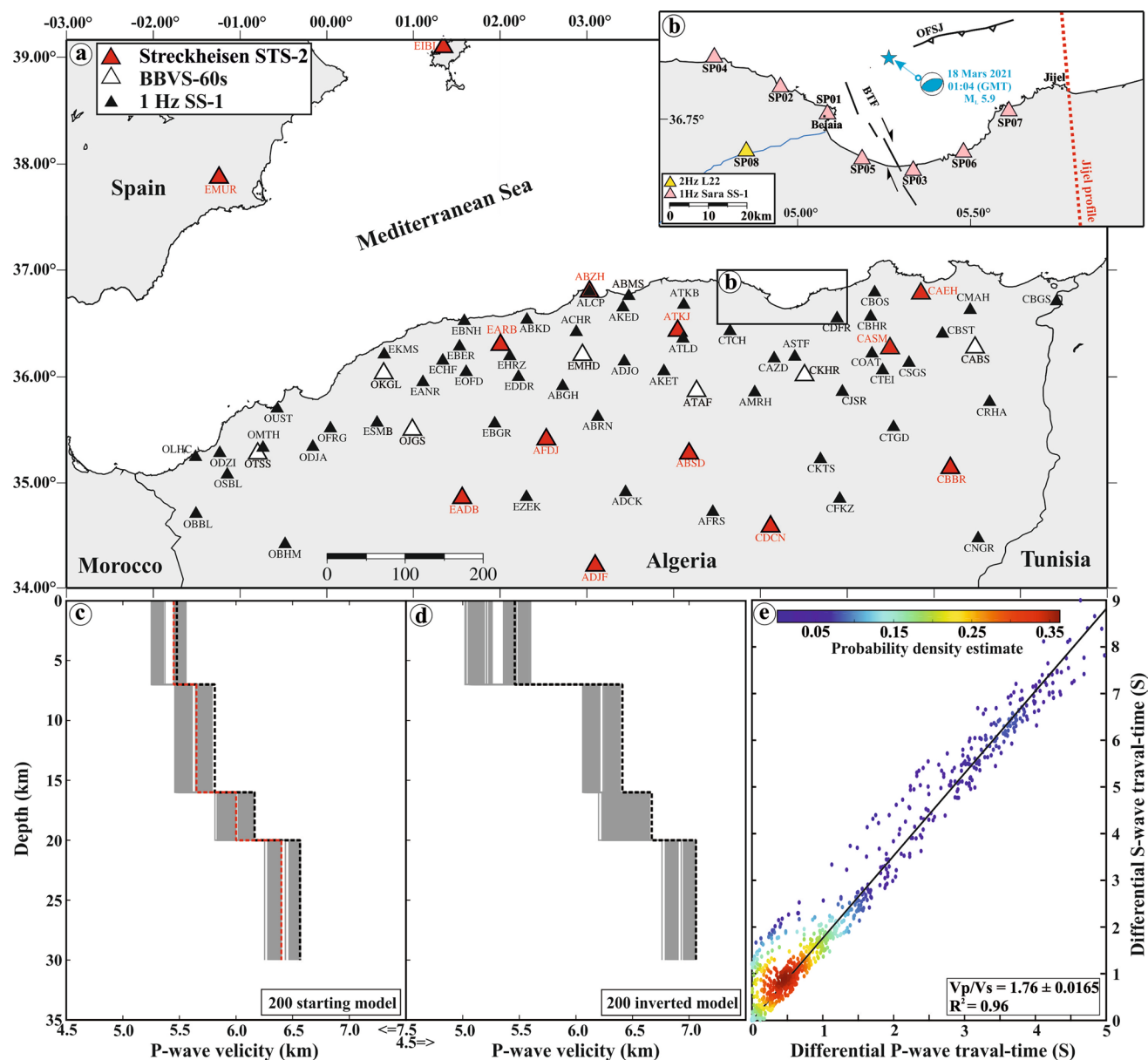
Fig. 2 a Distribution of permanent seismological stations operated by the ADSN. The stations are denoted by red and white triangles (broadband), and black triangles (short-period). **b** Distribution of the eight portable stations along the Bejaia Bay coastline. The station marked by a yellow triangle is equipped with an L22 sensor, while the remaining stations are equipped with Sara SS-1 sensors. The red dotted line represents the location of the SPIRAL Jijel profile (Mihoubi et al. 2014). **c** Represents the 200 starting models, with the red and black dashed lines representing the a priori velocity model and the best perturbed model that yielded the lowest residuals, respectively. **d** Illustrates the 200 inverted models generated from the starting model shown in (c), with the black dashed line representing the minimum 1D model. **e** Vp/Vs ratio in the Bejaia area determined using the modified Wadati method (Chatelain 1978)

(Mw), and focal mechanisms of the MS-2021, MS-2022, and one largest aftershock (hereafter LA) in 2021. To do that, we retrieve from the observed raw data the instrumental responses, convert them to ground velocity motions, cut a window of 100 to 200 s from continuous waveforms for each studied mainshock, apply a low-pass filter (0.02–0.07 Hz) to mitigate the effect of shallow velocity

structure heterogeneities, and produce the best fit between the observed and synthetic waveforms.

To extract the source parameters of the MS-2021, MS-2022, and LA, we conducted a *P*-wave spectral analysis using the procedure outlined in Abacha et al. (2019). The three-component records of each station (10 broadband stations) were corrected to a zero baseline and a common

instrument response. A time window was then selected for the desired phase (*P*-wave in this case) that started 0.1 s before the arrival time. Signal windows of varying lengths [2–8 s] were tested to determine a length that avoided contamination from other phases and maintained the resolution and stability of the spectra. We used a frequency range with signal-to-noise spectral ratios of > 5 for the source parameter estimation. After correcting for geometrical spreading and anelastic attenuation, the displacement amplitude spectrum was fitted by a theoretical spectrum assuming Brune's model with a circular dislocation (Brune 1970). The two unknown parameters to be determined in this method are Ω_0, the low-frequency spectral level, and f_c, the corner frequency (Hanks and Wyss 1972). These parameters are automatically selected to minimize the difference between theoretical and observed displacement spectra and to mitigate issues associated with visual determination. The average values for the seismic moment, source radius, and stress drop were then computed. The uncertainties were assessed using Archuleta et al. (1982).

We used the Win-Tensor program to analyze stress orientations and magnitudes (Delvaux 2012) from the previously computed focal mechanisms. This program assumes that the stress field is invariant and homogeneous in space and time in the study area, and that slip on a fault plane occurs in the direction of maximum resolved shear stress. Input data are preprocessed using the improved "Right Dihedron method" initially developed by Angelier and Mechler (1977), which provides the initial and approximate stress tensors that are used as a starting point in the rotational optimization method.

To assess the aftershock behavior, we applied three statistical laws: The Gutenberg–Richter law (Gutenberg and Richter 1944), the Omori–Utsu law (Utsu et al. 1995), and a temporal clustering (i.e., time concentration) (Hainzl et al. 2006). Their expressions are written as follows, respectively:

$$\log_{10}\left(N_{m>M}\right) = a - b*M, \tag{1}$$

where *N* is the number of earthquakes with magnitude ≥ *M*, *a* and *b* are constants. The parameter "*a*" is an indicator of the seismicity rate of the region, and "*b*" expresses the ratio between large and small earthquakes. The variations of b can be attributed to several factors, such as the heterogeneity of the environment or the depth of the source (Schorlemmer et al. 2005), and more importantly, the b-value is inversely proportional to the applied stress.

$$N(t) = \frac{dn}{dt} = \frac{K}{(t+c)^p}, \tag{2}$$

where *N(t)* represents the number of aftershocks versus time. *p* depends on the tectonic conditions of the region and generally varies between 0.8 and 2.5. *t*, *k*, and *c* are constants.

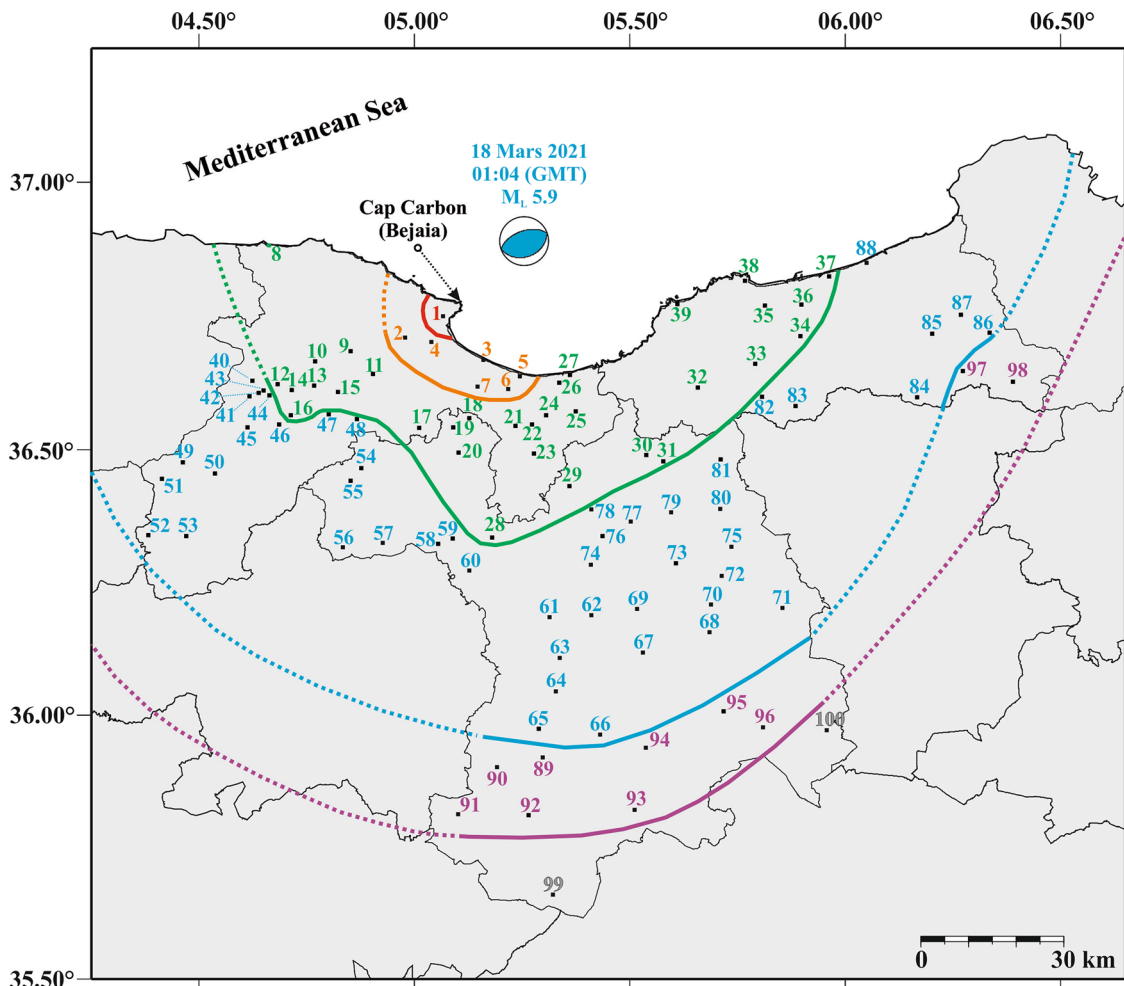$$d(\delta t) = Ce^{-\mu\delta t}\delta t^{-n}, \tag{3}$$

where *C* is a normalization factor, μ the frequency of independent seismicity (background rate), *n* the rate of seismicity linked to the mainshock (branching ratio), and δt the time intervals.

Results

Mainshocks: macroseismic effects, moment tensor, and physical parameters

The strong MS-2021 (M_L 5.9; CRAAG) occurred at midnight (00:04 UTC) and was preceded by a M_D 4.2 foreshock a few hours before, which nucleated in the MS-2021 proximity. The earthquake ground shaking caused a great panic among the population of Bejaia city of more than 100 000 inhabitants, and of several neighboring villages. Fortunately, no human casualties were reported in this densely populated city, located in the Babors Mountains' foothills. The isoseismal map drawn in Fig. 3, based on questionnaire responses collected by CRAAG, indicates that the earthquake was felt up to 150 km from the epicenter. However, multiple sources, including media news and social media platforms, have reported felt distances beyond 150 km, extending to cities such as Tizi Ouzou, Bouira, Skikda, and Algiers. Although the exact locations of these cities are not shown on the map, their inclusion is based on information gathered from external reports. The ancient city "the Casbah" was highly impacted by ground shaking, registering various damages in 2000 houses and social infrastructures, such as cracks, tiles falling off, and chimney collapses. A marine investigation along the Bejaia coast, made just after the MS-2021, does not show any evidence of coastal uplift as observed after the stronger 2003 Boumerdes earthquake Mw 6.8 (Fig. 3). Based on eyewitness reports, collected testimonies, and our field investigations, a maximum EMS-98 intensity of VII was assigned to the Bejaia city, i.e., pleistoseist. The isoseismal map (Fig. 3) provides a circular shape indicating, at first order, a radial energy dispersion, in agreement with the suspected E-W-trending main fault. In contrast, the MS-2022 (M_L 5.5, CRAAG), located in the same epicentral area, caused no damage. The MS-2021 has triggered a small tsunami, which was recorded by the Spanish tide gages, indicating a few centimeters of wave height.

The epicenter of the MS-2021 earthquake, situated offshore within Bejaia Bay, was determined to be at the geographical coordinates of 36.85°N and 5.22°E (this study). The locations reported by various seismological agencies, namely IGN, GEOPHONE, INGV, and GFZ, were found to be in close proximity to the coordinates provided by

Map: Mediterranean Sea; Cap Carbon (Bejaia); 18 Mars 2021, 01:04 (GMT), M_L 5.9

Intensity legend table:

VII	VI	V	IV	III	Ⅲ
1. Bejaia	2. Oued Ghir; 3. Tichy; 4. Tala Hamza; 5. Aokas; 6. Tizi N'berber; 7. Amalou	8. Beni Ksila; 9. El Kaseur; 10. Fenaia Ilmaten; 11. Amizour; 12. Tinbdar; 13. Timezrit; 14. Sidi Ayad; 15. Semaoun; 16. M'cinsa; 17. Kendira; 18. Ait Tizi; 19. Ait Naoual Mezada; 20. Bouandes; 21. Ait Smail; 22. Taskriout; 23. Kherrata; 24. Darguina; 25. Tamridjet; 26. Souk El Tenine; 27. Melbou; 28. Ain Roua; 29. Tizi N'Bachar; 30. Babor; 31. Serdj El Ghol; 32. Selma Benziada; 33. Texana; 34. Oudjana; 35. Kaous; 36. Taher; 37. El Kennar; 38. Jijel; 39. El Aouana	40. Akbou; 41. Chemini; 42. Souk Oufella; 43. Tibane; 44. LeFlaye; 45. Ouzellaguen; 46. Seddouk; 47. Beni Djellil; 48. Feraoun; 49. Ighram; 50. Akbou; 51. Beni Mellikreche; 52. Boudjellil; 53. Ighil Ali; 54. Beni Chebana; 55. Beni Ourtilane; 56. Guenzet; 57. Harbil; 58. Hammam Guergour; 59. Bougaa; 60. Beni Ouassine; 61. Ain Arnet; 62. Setif; 63. Mezloug; 64. Guellal; 65. Kasr El Abtal; 66. Bir Haddada; 67. Guedjal; 68. El Eulma; 69. Ouled Saber; 70. Guelta Zerka; 71. Belaa; 72. Tachouda; 73. Beni Fouda; 74. Le Ouricia; 75. Djmila; 76. Ouled Addouane; 77. Ain El Kebira; 78. Dehamecha; 80. Maaouia; 81. Ain Sebt; 82. Boudriaa Ben Yadjis; 83. Djimla; 84. Ouled Rabah; 85. Ouled Yahia Khedrouche; 86. Settara; 87. El Milia; 88. Sidi Abdelaziz	89. Ain Oulmen; 90. Ouled Si Ahmed; 91. Ouled Tebben; 92. Rosfa; 93. Ain Azel; 94. Ain Lahdjar; 95. Tella; 96. Hammam Sokhna; 97. Sidi Maarouf; 98. Ghebala;	99. Boutaleb; 100. Taya

(a) (b) (c) (d)

(e) Cap Carbon
(f) Weathering due to wave activity during storms; High tide; Low tide

Fig. 3 Isoseismal map of the 2021 Bejaia bay mainshock (MS-2021) according to the EMS-98 scale. The map illustrates the distribution of intensity levels, with Bejaia city experiencing a maximum intensity of $I_0 = $ VII. The numbers on the map indicate the corresponding questionnaires sent to local residents for intensity assessments. In the lower part of the figure, photographs (**a**, **b**, **c**, **d**, **e**, and **f**) depict observed damages, including structural damage to houses, block falls on the coastal road, and coastal changes along the Bejaia bay coastline (specifically at Cap Carbon). It is noteworthy that no topographic effects were observed

this study, as shown in Table 1. The famous Cap Carbon lighthouse is 15 km northeast of the epicenter. The focal mechanism was computed using *P*-wave first motion polarities on 50 vertical components. The optimal fit corresponds to (1) a thrust slip fault plane, striking ~ N70°, dipping 34° SSE, with a rake of 89°, and (2) a reverse slip fault plane, striking N251°, dipping 56° NNW, with a rake of 9°; this second plane is similar to the one determined by other agencies (Table 1). The MS-2021 waveform modeling reached the lowest variance reduction, 0.16 (84%), between observed and synthetic seismograms for a 9.1 km source depth. The estimated $M_0 = 9.7 \times 10^{17}$ N.m. corresponds to a moment magnitude Mw = 5.96 (~ 6.0). The moment tensor solution shows: One plane, which is a thrust fault, striking N71°, dipping 46° SSE, with a rake of 76°, and a second plane, striking N270°, dipping 45° N; yet consistent with an ~ EW thrust fault dipping NNW. This solution is compatible with the fault planes inferred from the *P*-wave first motion, with the various international agencies' independent results (Table 1), and with the LA solutions; both waveform modeling and *P*-wave first motion (Fig. 4). Furthermore, the resulting thrust faulting is also consistent with former earthquakes along the Algerian margin, such as the Boumerdes on May 21, 2003, the Algiers on August 1, 2014, and most recently the Jijel (east of Bejaia) on July 13, 2019, earthquakes. This focal mechanism is represented by a pure thrust, highlighting that the Algerian margin is continuously deformed by the forces resulting from the convergence between the oceanic crust of the Algero-Provençal basin and the continental crust of the Maghrebides. Figure 4 also displays the resolved moment tensor of the MS-2022, which exhibits a quite similar solution to that of the MS-2021 with a slight strike-slip component, whereas the solution inferred from the first *P*-wave onsets strikes slightly differently.

The physical source parameters extracted for the MS-2021, its LA, and the MS-2022 of the Bejaia Bay earthquake sequence are listed in Table 2, which shows an average corner frequency (f_c), seismic moment (M_0), source radius (*r*), stress drop ($\Delta\sigma$) values, multiplicative error factors *EM0* and *Efc,* the calculated moment

magnitude Mw, and displacement U values. Figure 5 presents an example of the *P*-wave displacement spectra at the ABSD station. The seismic moments and magnitudes following: M_0 (MS-2021) $= 9.1 \times 10^{17}$ N.m.; Mw (MS-2021) = 5.94; M_0 (LA) $= 5.3 \times 10^{16}$ N.m.; Mw (LA) = 5.1; and M_0 (MS-2022) $= 1.12 \times 10^{17}$ N.m.; Mw (MS-2022) = 5.34, are remarkably similar to those issued from the moment tensor inversion.
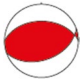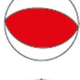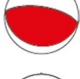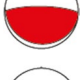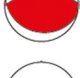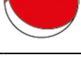
Aftershocks distribution and spatiotemporal evolution

We previously stated that a foreshock of magnitude M_D 4.2 preceded the MS-2021. The subsequent aftershocks activity lasted for nearly a month, from March 18 until April 15. A total of 500 events have been detected, yet only 475 events (95%) have been located (Fig. 6a). During this period, the LA, Mw 5.1, occurred 13 min later at 00:17 UTC. Its epicenter was located in the epicentral area close to the MS-2021 at a depth of 8.2 km. Ultimately, we selected the most accurate subset of events, keeping those having the criteria of: a root mean square residual (RMS) ≤ 0.3s; both horizontal error (ERH) and vertical error (ERZ) ≤ 3 km. These criteria yielded a dataset of 420 well-located events for further use. Consequently, the aftershocks horizontal distribution shows a surface of 15-km-wide × 35-km-long aftershock cluster.

From Fig. 6b, a dominant events number decline is clearly noticeable following the first day, when we registered around 200 events (40%), including the MS-2021 and its LA. The days after detected only a few aftershocks before returning to pre-MS-2021 levels. This could be explained by the energy mainly liberated on the first day, especially through the MS-2021 and its LA. Figure 6c shows that the aftershock magnitudes range between 2 and 3, and few events have a magnitude greater than or equal to 4.

Here, we examine the statistical behaviors for the 2021 Bejaia Bay seismic sequence. The cut-off magnitude in the Gutenberg–Richter relationships is Mc = 2.5. The magnitude distribution of events fitted by a Gutenberg–Richter law gives a *b*-value lower than 1 ($b = 0.83 \pm 0.07$). This result is consistent with the existence of an inverse relation between *b*-value and local stress level, as indicated by many laboratory measurements and field observations (Schorlemmer et al. 2005). Accordingly, large earthquakes are expected as signature for high-stress conditions. The *a*-value = 4.04 expresses a significant seismicity rate (Fig. 7a). The time distributions fitted by an Omori–Utsu's law show a decay with an exponent of $p = 0.95$, that is, ~ 1 (Fig. 7b). Typical signature decay of

Table 1 Mainshock locations and focal mechanism solutions obtained by this study and different seismological observatories

Source	Magnitude	Location		Depth	Nodal plane1			Nodal plane 2			M_0	Focal solutions
This study	Mw = 6.0	36.85	5.22	9.1	71	46	76	270	45	104	$M_0 = 0.97*10^{18}$	
USGS	$M_W = 6.0$	36.92	5.20	8	81	22	69	283	69	98	$M_0 = 1.37*10^{18}$	
GCMT	$M_W = 6.0$	36.83	5.29	12	85	28	75	282	63	98	$M_0 = 1.27*10^{18}$	
OCA	$M_W = 5.9$	36.90	5.20	11	275	55	90	95	35	90	$M_0 = /$	
GFZ	$M_W = 6.0$	36.89	5.16	16	98	22	88	279	67	90	$M_0 = 1.12*10^{18}$	
CPPT	$M_W = 6.2$	36.80	5.30	16	102	13	101	271	78	88	$M_0 = 2.27*10^{18}$	
INGV	$M_W = 6.2$	37.02	5.18	13	108	26	104	268	65	83	$M_0 = 2.22*10^{18}$	
IPGP	$M_W = 6.1$	36.92	5.21	8	117	28	117	267	65	76	$M_0 = 1.60*10^{18}$	

aftershock-like sequences (i.e., $p = 1$). The last statistical law (Fig. 7c) gives a value of $\mu = 2.80$ events per day, and a rate $n = 0.75$, this value indicates that 75% of the observed seismicity is linked to the mainshock, thus 25% is independent, i.e., background events. All the presented statistical elements point out a classical response of an aftershock-like sequence.

Finally, it is worth noticing that, we recorded thirty aftershocks of the MS-2022, mostly on one or two stations only, which impeded their location. Therefore, we characterized solely the MS-2022.

Aftershocks relocation, focal mechanisms, and stress tensor

Between March 18 and April 15 (days 2 to 30 after the MS-2021), 334 events out of 420 have been relocated (see Fig. 8). We also display the focal mechanisms of 40 key events, including the MS-2021 and LA (Table 3). The depths sources lie between 5 and 20 km. The cluster of aftershocks describes a 22 km long and 12 km wide structure. The events were located on the margin slop in the middle of Bejaia Bay. The NNW-SSE cross section, realized perpendicular to the fault plane resulting from

the focal mechanism, shows a plane dipping ~ 36°SE. This plane orientation is compatible with the dipping 34°SSE fault plane inferred from focal mechanism of the MS-2021 as well as with the dipping 46°SSE fault plane deduced from moment tensor inversion, with the MS-2021 hypocenter located in the central part. Therefore, the MS-2021 ruptured an ENE-WSE thrust fault, dipping SSE, situated at the western limit of the offshore WS thrust segment (Fig. 8a). Most of the aftershocks occurred above the mainshock plane, in the hanging wall, within a radius of approximately 10 km from the MS-2021 hypocenter. Figure 8 shows a small, distinct aftershock cluster dipping toward the north, in addition to the SSE dipping aftershock cluster. This cluster, represented by the circular shape in the cross section A1-B1 of Fig. 8, suggests the presence of a potential back thrust fault.

To rigorously assess the uncertainties associated with the relocated events obtained using the HypoDD method, we employed a bootstrapping technique, a powerful statistical method widely used in various scientific disciplines to estimate uncertainties. This technique involves resampling the data with replacement and calculating the statistic of interest for each resample. In our study, bootstrapping was applied to analyze the variability and reliability of the event
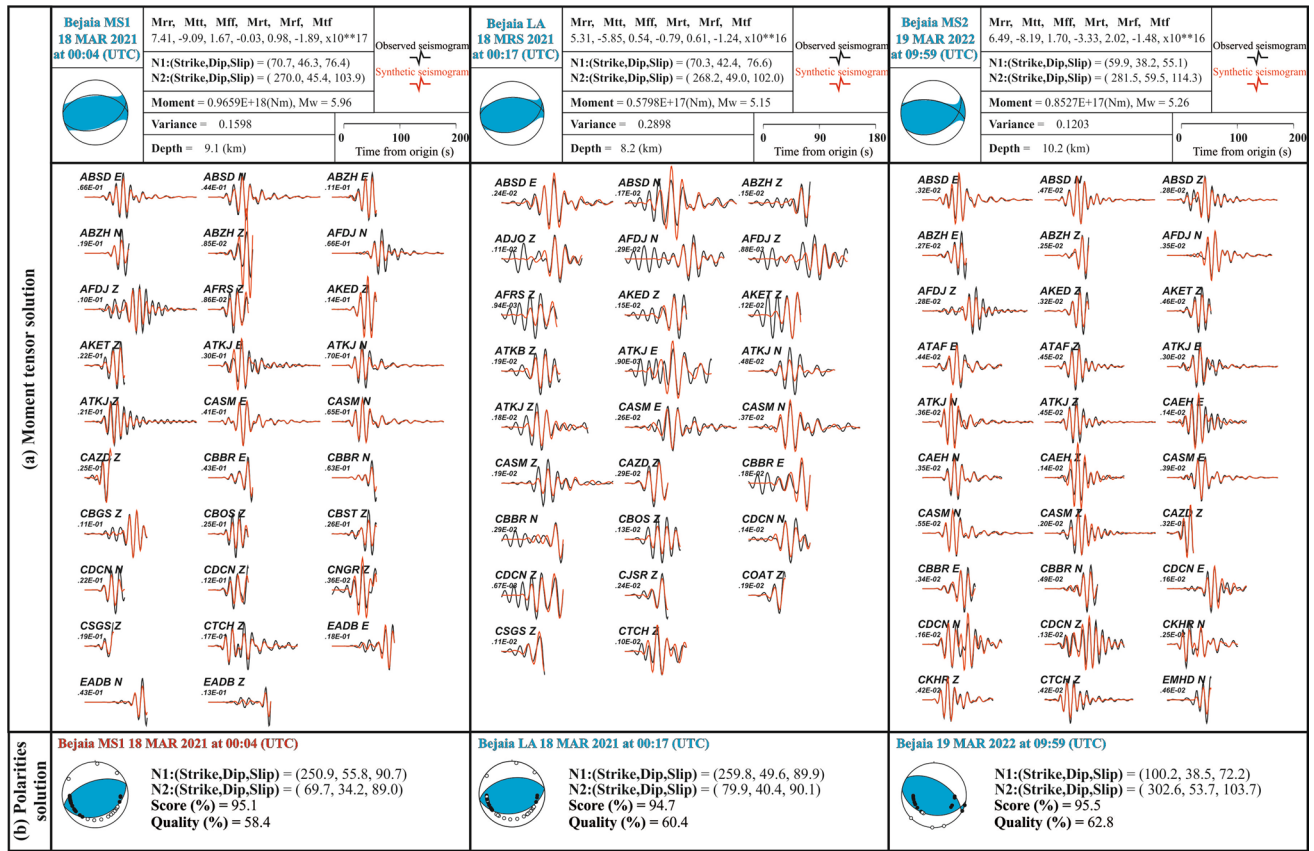
Fig. 4 (Top) Moment tensor solutions and best-fitted waveforms for the MS-2021 mainshock, its largest aftershock (LA), and the MS-2022 event. The observed data are represented by black lines, while the synthetic data are shown in red. The legend at the top provides information on the moment tensor parameters, resolved fault planes, scalar moment (M_0), moment magnitude (Mw), variance, and focal depth. The text labels on each waveform indicate the velocity in centimeters per second. (Bottom) Focal sphere solution derived from the first arrival P-wave polarities, along with the corresponding parameters for the MS-2021, LA, and MS-2022 events. The "score" and "quality" parameters assess the similarity between the observed polarities and those predicted by the model

Table 2 Average corner frequency (f_c), seismic moment (M_0), source radius (r), stress drop ($\Delta\sigma$), multiplicative error factors (EM_0 and Ef_c), and mean values of moment magnitude (Mw) and displacement (U) for the 2021 Bejaia mainshock (MS-2021), LA, and 2022 Bejaia mainshock (MS-2022)

Event	Time	f_c (HZ)	Ef_c	M_0 (Nm)	EM_0	$\Delta\sigma$ (Mpa)	R (m)	U (m)	Mw
MS-2021	18/03/2021 00:04	0.24	1.18	$9.07\ 10^{17}$	1.38	0.61	8663	0.13	5.94
LA	18/03/2021 00:17	1.14	1.27	$5.27\ 10^{16}$	1.18	4.00	1793	0.17	5.12
MS-2022	19/03/2022 09:59	1.01	1.12	$1.12\ 10^{17}$	1.26	5.91	2024	0.29	5.34

locations. Specifically, we generated 10 000 new datasets by randomly selecting observations from the original dataset (Fig. 8), allowing for the possibility of repeated selection. By recalculating the relative location error for each of these resampled datasets, we obtained a comprehensive distribution of location uncertainties. We used the median absolute deviation (MAD) of the bootstrap distribution of hypocentral coordinates to estimate the uncertainty. Unlike traditional measures of dispersion such as standard deviation, MAD is robust and less influenced by outliers or extreme values (Trugman et al. 2017 references therein). The resulting uncertainties in longitude, latitude, and depth were determined to be 397 m, 433 m, and 567 m, respectively (Fig. 8). These values indicate the variability and spread of the event locations, providing valuable insights into the reliability and confidence of our relocation results.
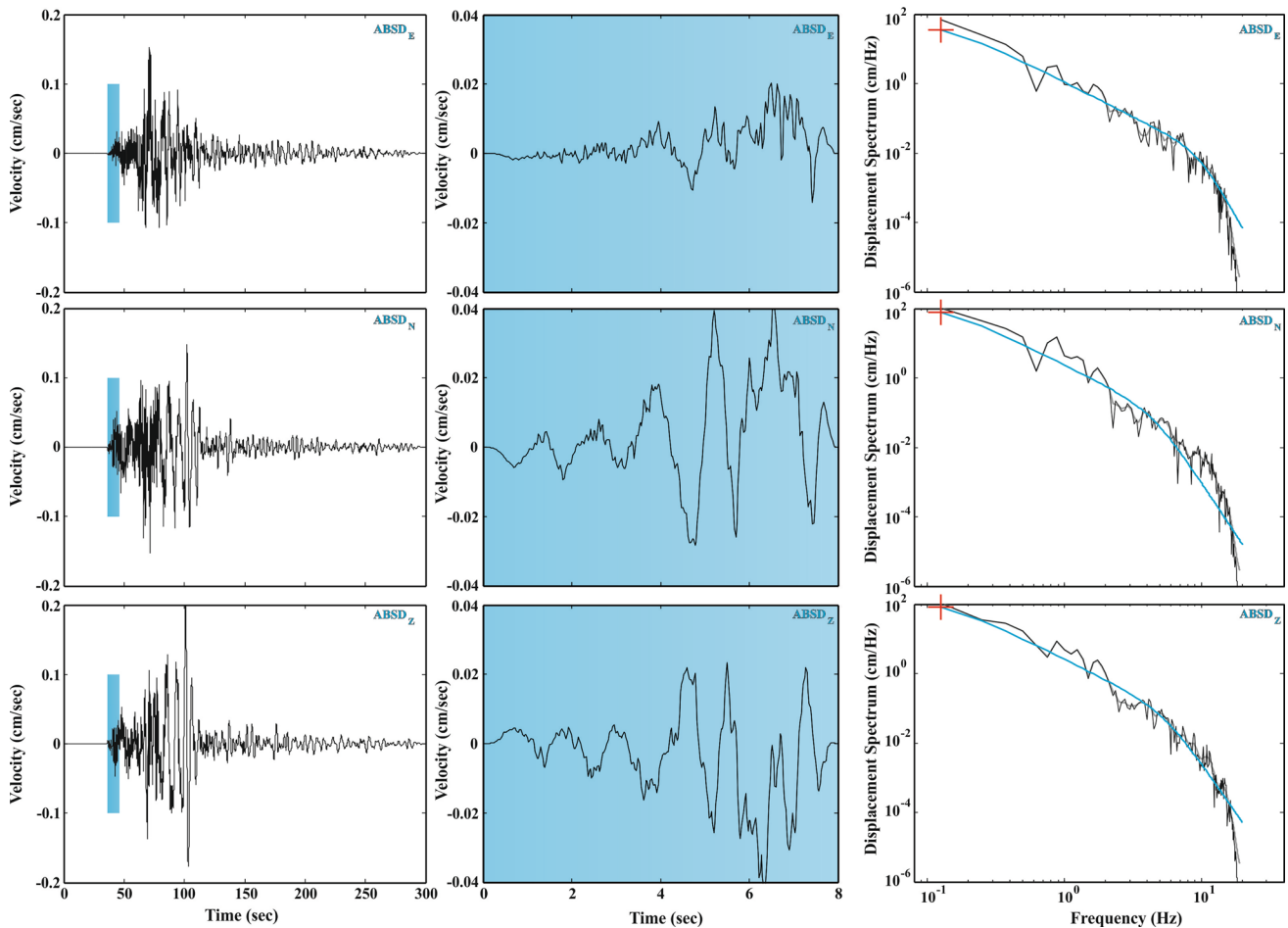
Fig. 5 Example displacement spectra at station ABSD. The left panel displays three-component instrumentally corrected velocity seismograms of the Mw 6.0 Bejaia mainshock (MS-2021) that occurred on March 18, 2021. The blue-shaded areas indicate the time windows corresponding to the *P*-wave trains, which are further magnified in the central panel. On the right panels, the displacement spectra of the P-wave seismograms are presented. The fitted spectra are shown in blue, while the observed spectra are represented by black lines. The gray lines represent the smoothed spectra. Additionally, the red crosses indicate the values of Ω_0 (lower frequency) and f_c (higher frequency)

In order to visualize the aftershocks sequence in its geologic environment within the Bejaia Bay, we acquired an interpreted NNW-SSE seismic reflection profile (Arab et al. 2016; Fig. 9a and b), which is near-parallel to our NNW-SSE cross section showing the fault dip. At first glance, the MS-2021 depth and focal mechanism matched perfectly the thrust fault labeled TF1 (Fig. 9b). The aftershocks depths occurred in the crystalline basement of the continental crust, without any events in the sedimentary layers at shallower depths (more details in the discussion).

Figure 10 shows the focal mechanisms inversions in the epicentral area (Fig. 9). Stress inversion indicates a sub-vertical σ_3 orientation (plunge N85E/azimuth 184°), and sub-horizontal σ_2 (plunge N01E/azimuth 075°) and σ_1 (plungeN04E/azimuth 345°). This analysis indicates that the current stress field is characterized by a contractional regime ($R' = 2.99 \pm 0.24$; Fig. 10), in agreement with the NNW-SSE Africa–Eurasia convergence orientation (Bougrine et al. 2019) and with previous studies around LKB (Bendjama et al. 2021, Yelles-Chaouche 2021; Boulahia et al. 2021).

Discussion

After the Boumerdes earthquake on May 21, 2003, with a magnitude Mw 6.8, the current Bejaia Bay earthquake on March 18, 2021, with a magnitude Mw 6.0, is the largest offshore earthquake in the past 20 years. The occurrence of such a strong earthquake in northern Algeria is rare, with an average of three to five per century. Nevertheless, this
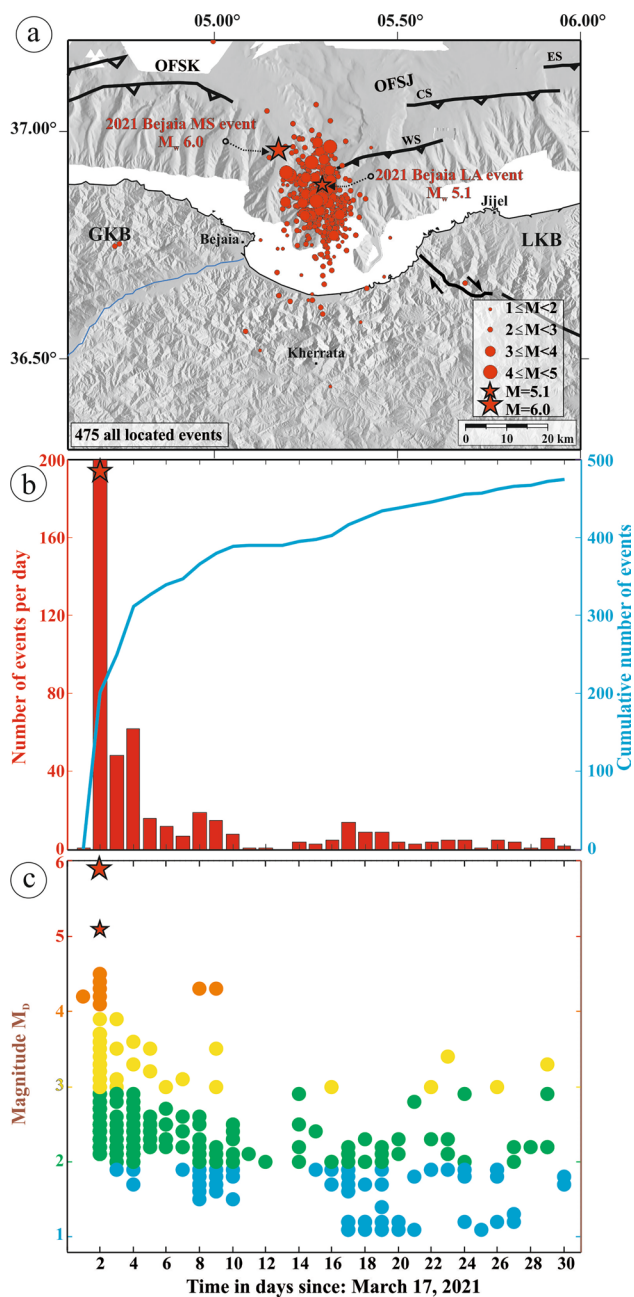
Fig. 6 **a** Horizontal distribution of the 475 located events recorded during the period from March 17 to April 15, 2021. **b** The number of located events per day is represented by the red histogram, while the cumulative number of events is shown by the blue curve. **c** The daily distribution of M_D (Magnitude of Duration) values is depicted. The plain dots are color-coded based on the magnitude range of the events, ranging from blue ($M_D < 2$) to red ($M_D \geq 5$)

earthquake is an expression of the ongoing processes of deformation at the Algerian margin as a result of the oblique convergence of Africa and Eurasia. The offshore location of the MS-2021 epicenter, where a series of quakes with

magnitudes around Mw 5 have regularly occurred since 2012, raises concerns about the underlying mechanics of faulting and the factors that control seismic activity. For example, in the Bejaia–Jijel area, a large amount of strain build-up and simultaneous rupture on several segments are highly plausible; the historical earthquake that struck Djidjelli on August 21–22, 1856 (I_0: X) complies with this scenario (Yelles-Chaouche et al. 2009).

Starting from the Oligocene times, the eastern Algerian margin has been subjected to multiple tectonic phases, evidenced by significant vertical motions in both directions and successions of crustal extension and compression (Jolivet and Faccenna 2000), leading to the development of structures with variable orientations and kinematic histories and, therefore, variable potential for reactivation under the present stress conditions. In order to provide a seismotectonic interpretation of the Bejaia Bay seismic sequence and an earthquake-fault association, we compared the MS-2021 focal solutions and aftershock locations to the geometry of the margin fold-and-thrust faults. The structure of the eastern Algerian basin was defined by Arab et al. (2016) using a combination of new set of offshore deep penetrating seismic, conventional MCS sections, and wide-angle seismic data. In the deep part of the lower margin the south-dipping ramps were well evidenced, supporting previous interpretations (Yelles-Chaouche et al. 2009). They form en echelon segments parallel to the margin and express the antithetic inversion of the margin comparatively to the Alpine north-dipping thrusting (Mock and Herwegh 2017). The en echelon pattern of the thrusts results from the reactivation of the NW–SE wrench faults during inversion (Arab et al 2016). The MS-2021 focal mechanism shows roughly E-W striking planes, one plane gently dips toward the south (thrust fault), and the second steeply dips toward the north (a reverse fault). The epicenter of the earthquake indicated that the seismogenic source is located on the OCT (Ocean-Continent Transition), which is less than 40 km from the shoreline (Mihoubi et al. 2014). The overthrusting of the Kabylian basement is accommodated at the OCT (Klingelhoefer et al. 2022). Aftershocks concentrate within the Lesser Kabylian basement, their hypocentral distributions depict an alignment S-dipping with 36°. The folding of Pre-Messinian units is the most compelling evidence for crustal shortening at the foot of the Algerian margin off Jijel and the presence of a thrust-fault emerging from the hinge of the Lesser Kabylian basin and basement rise (Mihoubi et al. 2014). Therefore, the tectonic structure that best fits these requisites seems to be the upper-thrust blind fault south-dipping labeled as TF1 (Fig. 9). Furthermore, five main south-dipping ramps that exert a strong control on the seafloor morphology and depositional patterns were identified offshore Boumerdes (central
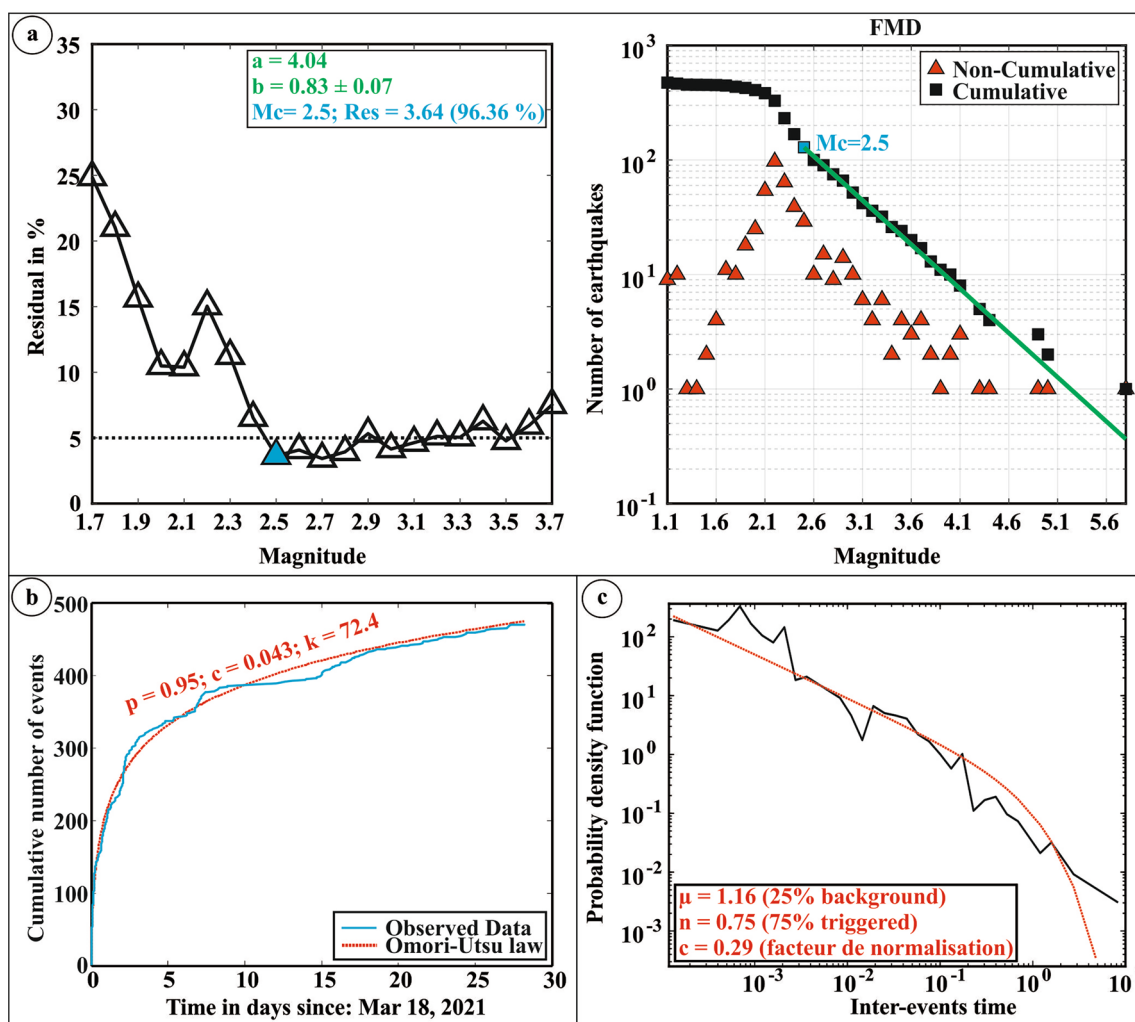
Fig. 7 **a** Gutenberg–Richter law of the 2021 Bejaia seismic sequence. The left panel represents the minimum residual, which corresponds to the value of Mc. The right panel represents the frequency-magnitude distributions. **b** Cumulative number fitted by the Omori–Utsu law. **c** Probability density of time intervals between seismic events

Algerian margin), where two of them generated the Boumerdes earthquake on May 21, 2003, Mw 6.8 (Déverchère et al. 2005). The historical Djidjelli earthquake rupture on August 21–22, 1856 (I_0: X) was simulated on three south-dipping segments (ES, CS, and WS; Fig. 11) (Yelles-Chaouche et al. 2009). The active faults evidence the underthrusting of the Neogene oceanic domain below the Algerian margin, which might represent an incipient stage of subduction (Auzende et al. 1975).

Earthquakes commonly occur either as mainshock–aftershock or as seismic swarms. Each one highlights different triggering process. The Bejaia–Bay aftershock activity exhibits classical patterns of aftershock sequences by showing (1) Aftershock distributions fit the Omori-law decay in the rate of events with time (p value = 0.95);

(2) Their magnitude follows a Gutenberg–Richter law (b-value = 0.83); (3) The temporal clustering (n-value = 0.75, which means 75% are triggered events); (4) No migration pattern underlined, the MS-2021 likely reactivates the entire area quasi-instantaneously; and (5) The aftershocks hypocenters are located in a radius less than 10 km from the MS-2021 hypocenter, which ruptured a segment fault of ~ 18 km (Table 2). From the provided elements, the sequence shows aftershock-like behavior, which is caused primarily by stress changes due to slip dislocation during the mainshock or its afterslip (Yukutake and Iio 2017). Therefore, the aftershocks are likely to be triggered by static stress transferred from the mainshock (Stein 1999); most of the aftershocks represent the rupture of fractures surrounding the mainshock fault, rather than the re-rupture of the
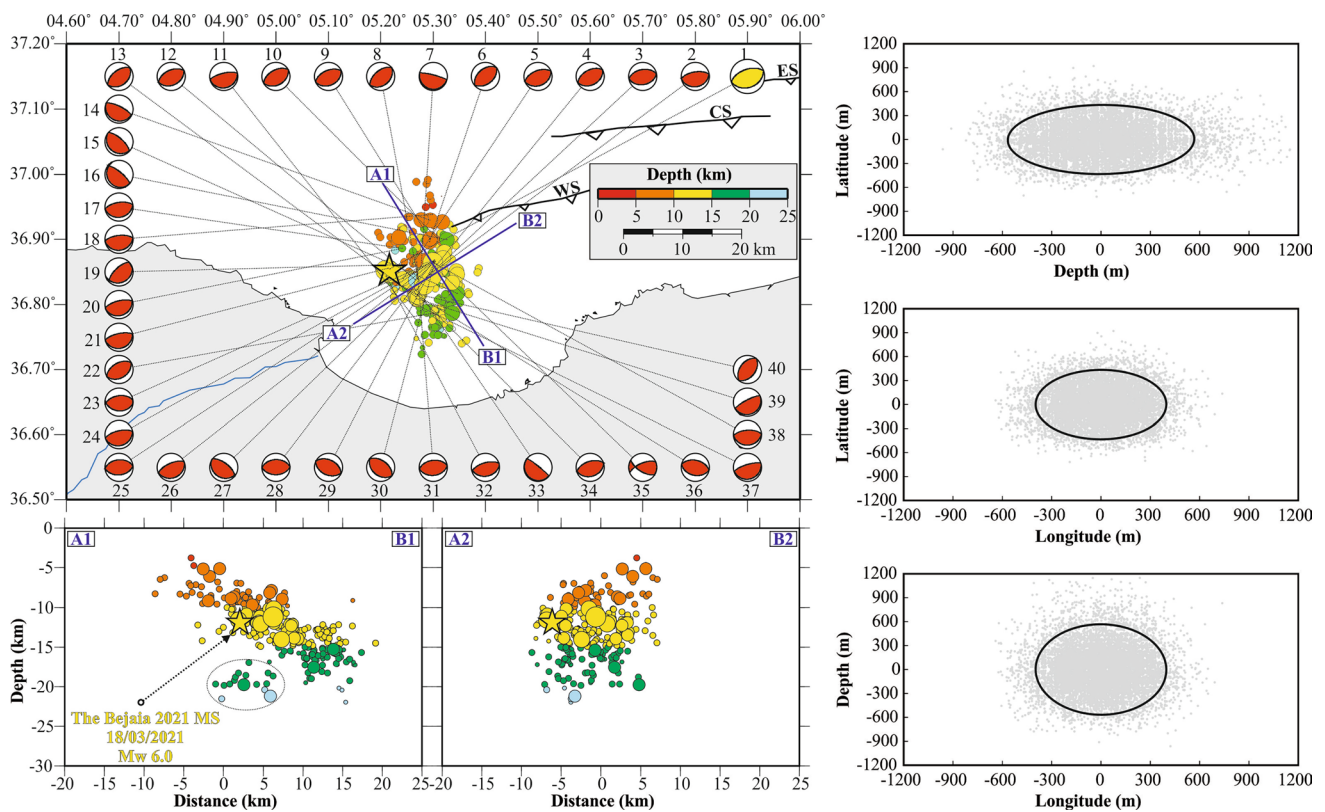
Fig. 8 Horizontal and vertical distribution of relocated events and focal mechanisms. The figure displays the horizontal distribution of the relocated events and provides two cross sections, A1-B1 and A2-B2, showcasing the vertical distribution. The color scheme indicates the depth of the events. The focal mechanisms of 40 key events, corresponding to the numbers in Table 3, are also depicted. Relative location uncertainties obtained via 10,000 bootstrap resampling of the hypocentral coordinates are shown, with the contour representing the 95% confidence ellipsoid in the x (E–W), y (N–S), and z (up-down) directions

mainshock fault, participating to equilibrate the stress after earthquake perturbation. The process behind the aftershocks located close to the mainshock is the coseismic Coulomb stress transfer. Furthermore, two previous studies (Boulahia et al. 2021 and Yelles-Chaouche et al. 2021) highlighted positive charge loaded from coseismic Coulomb stress transferred from approximate earthquakes (Fig. 12). Moreover, the oblique stress compression (N345°E) inferred from focal mechanisms matches the NNW-SSE Africa–Eurasia convergence direction (Bougrine et al. 2019), which suggests that the stress tensor is controlled by the overall regional stress field.

The Bejaia–Babors Transverse Zone (Boulahia et al. 2021), located between LKB and GKB, is one of the NW–SE fault zones that dissect the lateral continuity of the margin thrust front. The transverse zone includes two major vertical shear zones, BTF (Babors Transverse Fault) and Aftis Fault with its prolongation offshore (Arab et al. 2016 and Abacha et al. 2023). Both constitute, respectively, the westernmost and easternmost limits of the ruptured thrust segment (Fig. 11). Thomas (1990) gives a thorough explanation of the factors that could affect where transverse zones are located in thrust systems, including the existence of deep pre-existing lineaments, the pre-thrusting deformation of cover layers above deep faults, and changes in mechanical stratigraphy. The best candidate for controlling the origin of the Bejaia–Babors Transverse Zone can be identified in the presence of pre-existing lineaments. Arab et al. (2016) identified on the field and offshore a set of NW–SE dextral strike-slip faults in the northeast Algerian margin, with vertical components acting primarily during the synrift phase, and they predicted their reactivation during the inversion. Transverse zones structures are the site for the development of tear faults and lateral ramps that interact with frontal ramps and thrust-related folds, causing abrupt along-strike changes in the lateral continuity of thrust-stacks (Zanchi et al. 2012), and as previously stated the en echelon pattern of the northeastern Algeria offshore thrust ramps was shaped by the reactivation of the NW–SE wrench faults during inversion. The Bejaia–Babors transverse faults are

Table 3 Fault plane solutions for the 2021 Bejaia mainshock (MS-2021), LA, and 38 key aftershocks of the Bejaia earthquake sequence

No.	Date	Origin time	Md	Location		Depth	Nodal Plane 1			Nodal Plane 2			Score	Quality
				Lat (N)	Lon (E)	Km	Strike (°)	Dip (°)	Rake (°)	Strike(°)	Dip(°)	Rake(°)		
1	18/03/2021	00:04	5.9	36.8543	5.2175	11.79	69.7	34.2	89.0	250.9	55.8	90.7	95.1	58.4
2	18/03/2021	00:13	4.1	36.8418	5.2866	10.17	80.8	25.8	89.6	260.5	64.2	90.2	81	66.4
3	18/03/2021	00:17	5.2	36.8464	5.2941	11.22	79.9	40.4	90.1	259.8	49.6	89.9	94.7	60.4
4	18/03/2021	00:36	3.2	36.8218	5.2666	08.95	62.3	38.1	89.7	242.6	51.9	90.2	87.5	67.2
5	18/03/2021	01:04	3.2	36.8399	5.2425	11.11	67.1	33.5	89.0	248.4	56.5	90.2	94.9	74.1
6	18/03/2021	01:28	3.0	36.8967	5.2928	08.66	51.4	45.0	90.0	230.4	45.0	89.2	81.5	61
7	18/03/2021	01:30	2.7	36.8587	5.2776	09.97	284.5	81.5	89.9	105.2	8.5	90.7	100	69.4
8	18/03/2021	01:35	3.3	36.8397	5.2707	08.14	50.8	34.3	89.9	105.2	55.7	90.7	94.4	70.4
9	18/03/2021	01:38	3.7	36.9011	5.2942	08.87	65.3	35.3	88.8	246.8	54.7	90.8	100	69.2
10	18/03/2021	02:14	2.9	36.9024	5.3083	08.49	60.5	37.2	89.3	241.3	52.8	90.5	65	56
11	18/03/2021	03:29	2.5	36.7721	5.2713	18.11	77.6	18.3	91.1	256.4	71.7	89.6	52	54.4
12	18/03/2021	04:27	2.1	36.8386	5.2654	09.90	64.4	36.8	89.1	245.5	53.2	90.7	78.6	64.4
13	18/03/2021	06:46	3.0	36.8120	5.2670	12.12	51.6	34.7	89.3	232.5	55.3	90.5	82.6	63.6
14	18/03/2021	16:21	4.4	36.5713	5.1743	12.88	112.8	16.2	86.8	296.1	73.8	90.9	96.6	78.7
15	18/03/2021	17:22	3.3	36.8171	5.3462	17.55	129.0	20.6	87.8	311.4	69.4	90.3	80	61.1
16	18/03/2021	19:05	3.7	36.8995	5.3266	19.75	153.3	16.2	113.3	309.1	75.2	83.4	87.5	60.5
17	18/03/2021	19:16	3.6	36.8861	5.2411	19.82	81.5	25.9	90.7	260.8	64.1	89.7	68.4	53.6
18	19/03/2021	01:32	2.8	36.8847	5.2338	17.55	255.7	68.7	92.2	69.8	21.4	84.5	58.2	59
19	19/03/2021	02:23	3.1	36.9385	5.2988	18.35	263.2	66.8	89.9	83.6	23.2	90.3	83.3	58.5
10	19/03/2021	08:33	3.5	36.8618	5.2497	17.93	72.4	23.4	87.2	225.5	66.6	91.2	80	56.4
21	19/03/2021	20:44	2.9	36.8559	5.2138	11.07	257.4	70.0	90.2	76.9	20.0	89.5	86.2	70.4
22	19/03/2021	22:11	2.9	36.7886	5.3111	13.10	60.0	90.0	240.0	52.0	90.0	171.8	100	72
23	19/03/2021	22:25	2.9	36.8664	5.3007	11.88	97.4	36.8	89.1	260.5	53.2	90.7	78.6	66.2
24	20/03/2021	01:42	2.6	36.8665	5.3005	11.62	75.0	22.6	88.9	256.2	67.4	90.5	84.2	69.3
25	20/03/2021	01:51	3.6	36.8682	5.3024	11.91	85.7	44.0	91.4	263.7	46.0	88.6	94.4	67.1
26	20/03/2021	02:06	2.8	36.8663	5.3017	12.03	67.8	23.1	91.4	246.3	66.9	89.4	94.4	63.1
27	20/03/2021	02:32	2.8	36.8643	5.3011	11.79	120.3	25.1	84.0	306.9	65.0	92.8	74.4	65.6
28	20/03/2021	03:37	2.9	36.8652	5.2995	11.97	268.2	44.7	89.4	89.0	45.3	90.6	100	66.5
29	20/03/2021	04:17	2.8	36.8669	5.3037	11.72	114.0	43.4	88.9	295.5	46.6	91.0	94.4	65.9
30	20/03/2021	06:17	3.3	36.8647	5.3024	11.87	128.8	38.5	92.2	306.1	51.5	88.3	84.2	62.2
31	20/03/2021	11:32	2.7	36.8158	5.2702	12.25	39.2	44.2	91.3	217.5	45.8	88.8	80.4	70.4
32	20/03/2021	22:37	2.7	36.8652	5.2687	13.59	84.5	40.6	91.9	262.0	49.5	88.4	93.3	65.5
33	22/03/2021	00:56	2.5	36.8438	5.2098	10.12	80.5	35.5	89.0	253.8	63.9	89.2	61.1	89.9
34	23/03/2021	09:12	3.1	36.8233	5.2691	10.21	128.2	5.5	89.6	308.6	84.5	90.0	84.8	68.9
35	23/03/2021	17:49	2.6	36.8193	5.2635	12.26	72.5	34.5	90.0	252.5	55.5	90.0	91.7	90
36	24/03/2021	04:57	2.6	36.8621	5.2979	11.95	122.0	63.9	179.8	247.0	66.4	90.4	66.7	58.3
37	24/03/2021	22:08	2.1	36.8086	5.2451	12.50	73.0	15.3	90.1	252.9	74.7	90.9	92.2	70.6
38	24/03/2021	23:01	2.2	36.8341	5.2290	08.75	281.4	48.7	88.7	103.3	41.3	91.4	991.7	70.6
39	24/03/2021	23:23	4.3	36.8649	5.2992	12.08	86.0	26.5	89.7	266.4	63.5	90.2	84.1	69.3
40	01/04/2021	16:22	3.0	36.8091	5.2688	12.12	63.1	11.8	90.6	242.5	78.2	89.9	92	68.6

The parameters 'Score' and 'quality' are defined in Fig. 4

currently activated as oblique right-lateral strike-slip faults, attested by the occurrence of several moderate earthquake sequences such as the 2012–2013 seismic sequence with three events having $5.0 \leq Mw \leq 5.2$ along BFT fault and an Mw 5.0 event in El-Aouana on January 24, 2020, which ruptured a small segment of Aftis fault. The question that arises is whether this intense seismic activity along the transverse system contributed to the failure of MS-2021
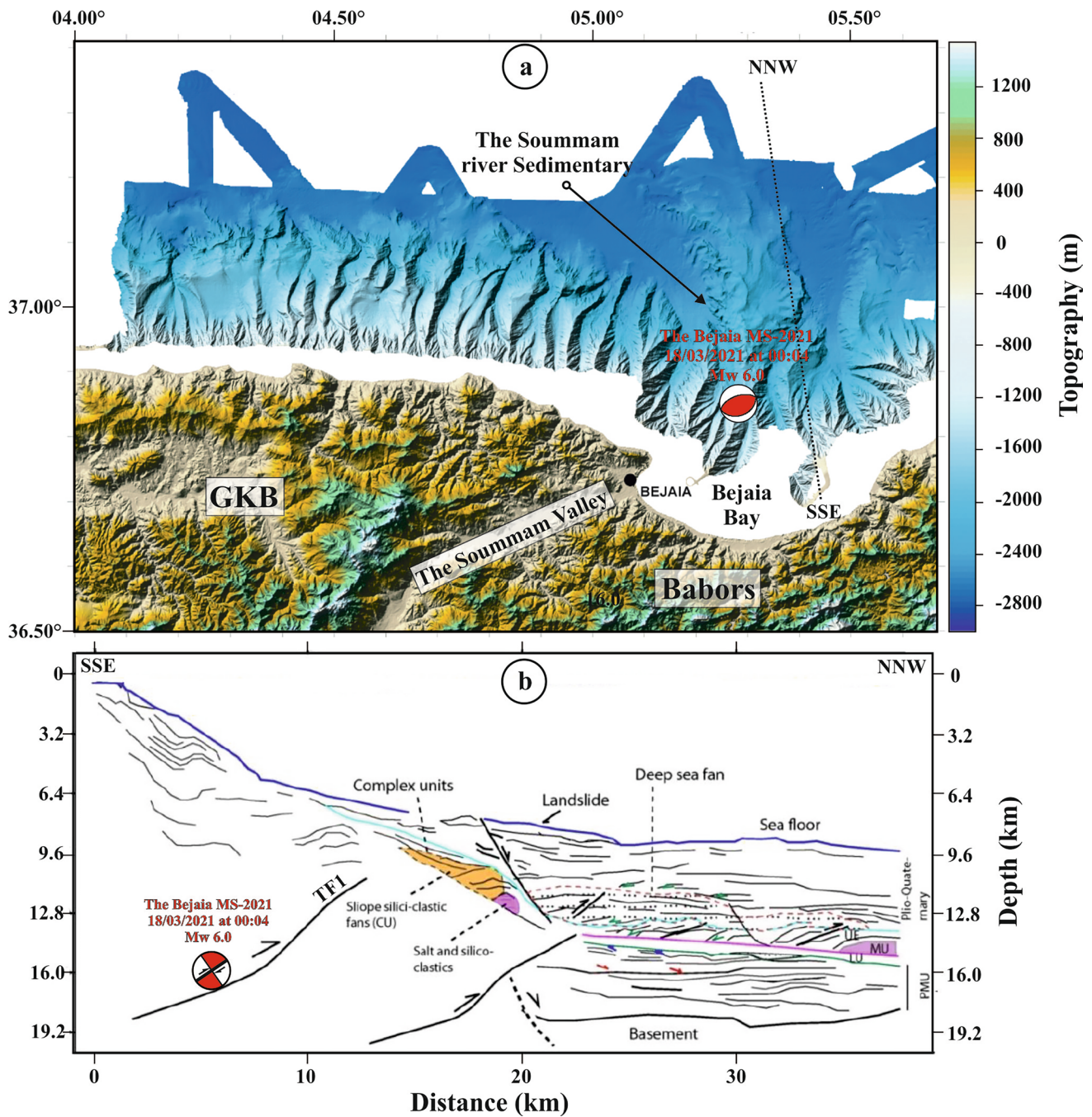
Fig. 9 a Bathymetry and topography of the Bejaia area, encompassing the GKB, Babors, and Bejaia Bay. The resolution is at 50m intervals (modified from Domzig 2006). The dotted black line corresponds to the southern segment of the P1 seismic section off Bejaia, as described by Arab et al. (2016). **b** Structural and stratigraphic interpretation of section P1, adapted from Arab et al. (2016), with the addition of a sectional view depicting the focal sphere of the MS-2021 earthquake. The depth units have been converted from two-way travel time (twt) to kilometers

and MS-2022 a year later. Stress transfer between thrusts and tear faults has been observed in many earthquakes; for example, the 2003 Mw 6.8 Boumerdes earthquake (Lin et al. 2011). They found that slip-on tear faults linking en echelon thrust sources are strongly promoted by an adjacent thrust earthquake. Magistrale and Day (1999) indicated that the presence of a tear fault favors the jump of dynamic rupture from the source earthquake thrust fault to its adjacent

Fig. 10 Stress inversion results displaying selected focal planes projected onto the lower hemisphere using Schmidt stereographic projections. The violet lines represent the focal planes, while the three principal stress axes (σ1: circle, σ2: triangle, and σ3: square) and the horizontal stress axes (SHmax: violet arrows and SHmin: green arrows) are indicated. Stress symbols indicate the orientation of the horizontal stress axes. The histogram illustrates the distribution of the misfit function F5, weighted linearly by the event magnitudes. QRfmt refers to the Quality Ranking for focal mechanism solutions in stress data records obtained from formal stress inversions. The Frohlich diagram is employed to assess the faulting types, denoted as SS (strike-slip), TF (thrust), U (unknown), NF (normal), TS (thrust to strike-slip), and NS (normal to strike-slip). The stability of R' and σ1 values
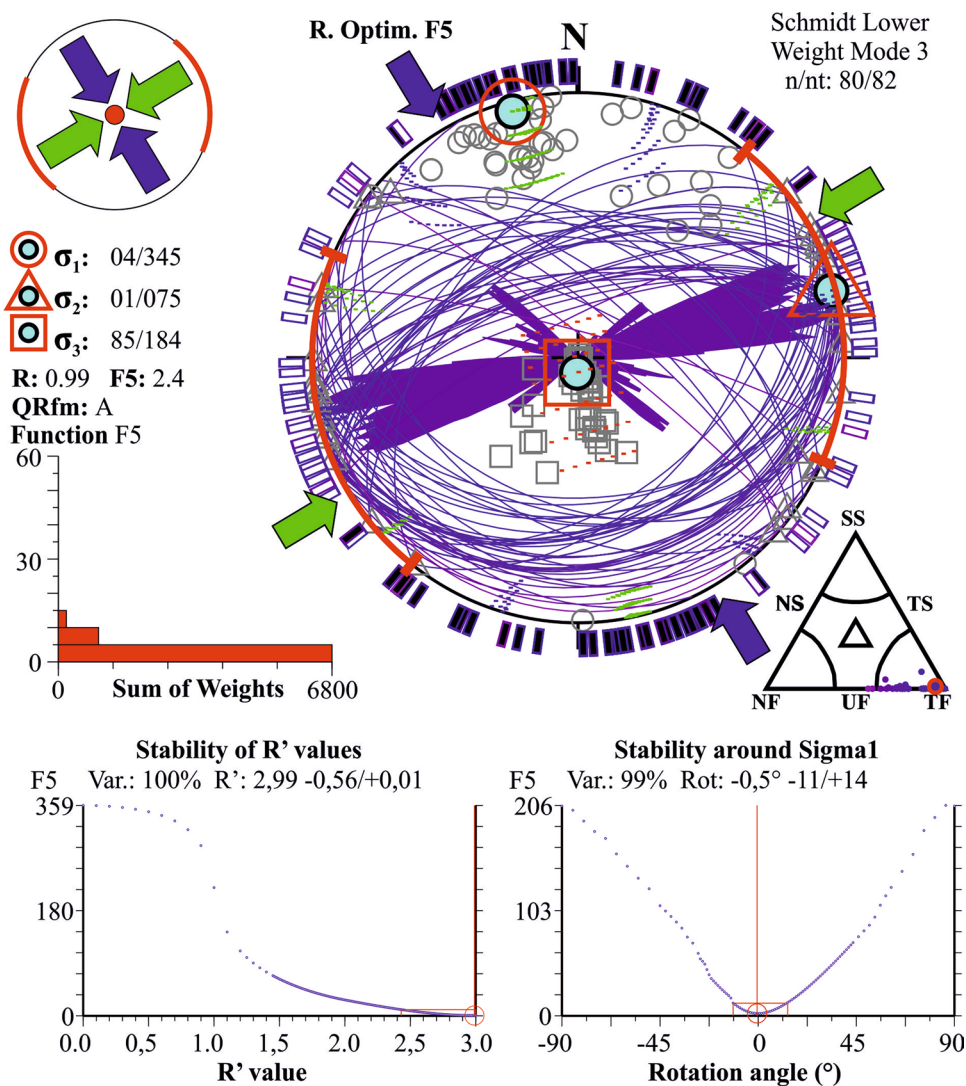
thrust fault segments, which might explain the mechanism at play for the rupturing of the three segments during the Djidjelli earthquake on August 21–22, 1856. According to Akoğlu et al. (2018), tear faults either act as a barrier to impede the rupture or instead help it to jump to adjacent thrust segments. So did the Bejaia–Babors transverse system act as a barrier, preventing the rupture from jumping to the thrust faults in the west—toward the Great Kabylian thrusts; offshore and the one inland, fringing the Soummam Valley to the north? Based on historical catalogs, it could be the case, no strong or destructive earthquakes have ever been recorded on the thrust faults bordering the GKB offshore and inland. On the other hand, is the worst-case scenario realistic? Which involves the rupture of several en echelon thrust segments east and west of the transverse system, given

the short time covered by the historical catalogs and the absence of Paleo-earthquake evidence, it could be the case either. What is certain is that large ruptures on either the east Lesser Kabylian thrusts offshore or the west Great Kabylian thrusts (both offshore and its parallel inland) would have a significant impact on several densely populated districts. Therefore, the interplay between these fault systems required further seismotectonic investigations.

The installation of the Algerian Digital Seismological Network in 2007 and beyond represented a significant improvement in earthquake monitoring capabilities for the country, allowing for more accurate, timely detection, and a comprehensive understanding of earthquake activity in different regions, especially around the Lesser Kabylian Block, following a series of moderate events in the last few years.
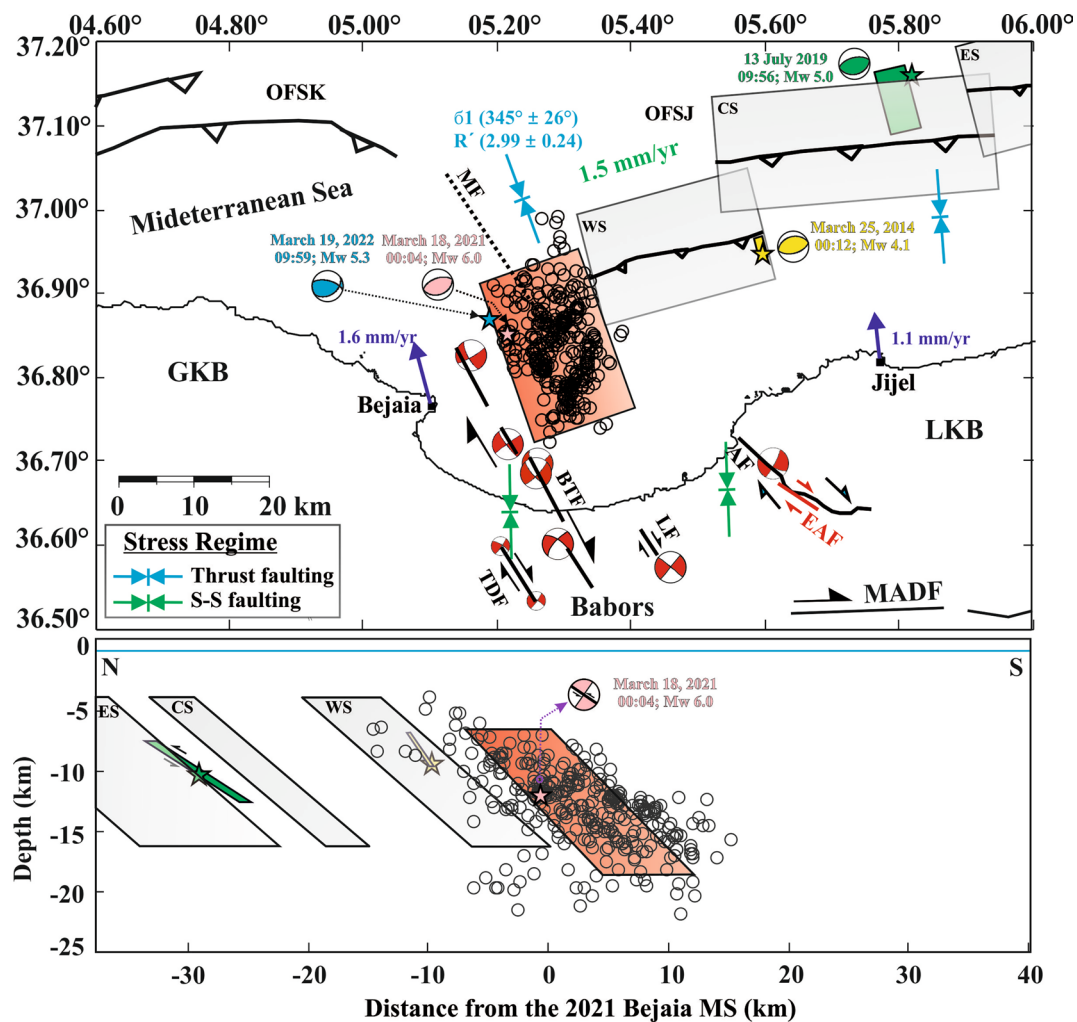
Fig. 11 Tectonic context of the study area, highlighting the newly identified Bejaia segment (red rectangle) determined in this study. The 2019 and 2014 earthquakes (Yelles-Chaouche et al. 2021) are represented by green and yellow, respectively. The ES, CS, and WS fault segments (Yelles-Chaouche et al. 2009) are depicted by gray rectangles. The focal mechanisms of the main events and the primary active faults in the study area, as reported by Boulahia et al. (2021) and Abacha et al. (2023), are also shown. The green number represents the horizontal displacement rates along the offshore faults in mm/yr. The violet arrow denotes the GPS velocity based on Bougrine et al. (2019). The main parameters of the stress tensor are presented in blue

The seismic analysis of these sequences provides valuable insights into the underlying geology and tectonic processes governing earthquake activity. The recently computed focal mechanisms in the zone between lesser and greater Kabylian blocks show right-lateral strike-slip faulting on oblique faults, which led to the identification of an unknown NW–SE transverse fault system separating the two blocks (Boulahia et al. 2021 and Abacha et al. 2023), breaking in this area a long-lasting consensus that attributes the seismic activity to the NE-SW Kharrata reverse fault (Boulahia et al. 2021 and references therein). The moderate events that occurred offshore on the LKB westernmost thrusts (Yelles-Chaouche et al. 2021) mark the instrumental era of seismic activity, along with the current Bejaia Bay sequence, which partially fills a seismic gap between the previous thrusts and the oblique transverse system. This last connects the transverse system to the major dextral Mcid Aïcha-Debbagh fault (MAD); according to Bougrine et al. (2019), its length is about 400 km, and numerous moderate seismic sequences took place along this major structure (Bendjama 2022), which allow disclosing the mechanism of the strain partitioning in an oblique convergence context: the strike-slip
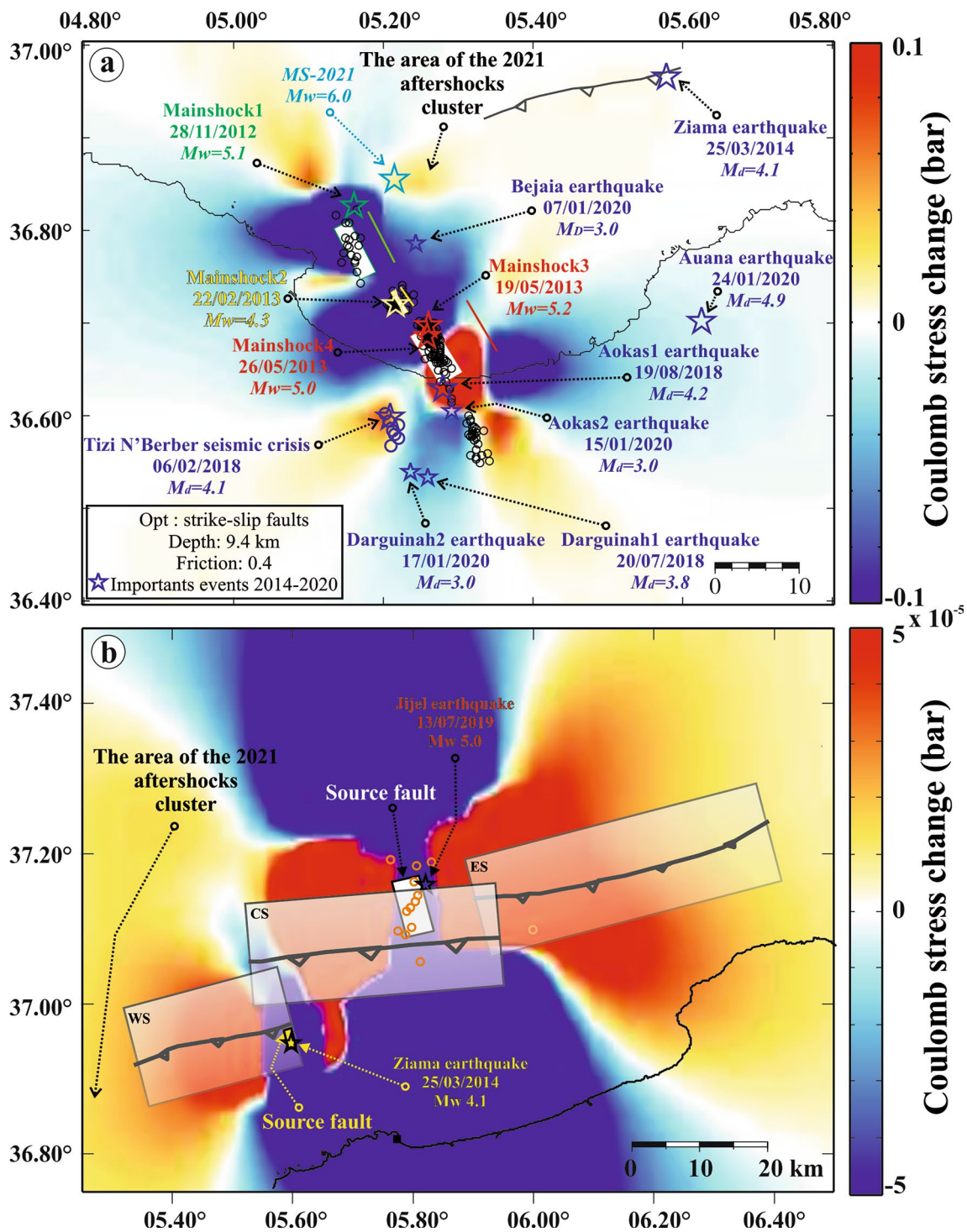
Fig. 12 Calculated Coulomb stress changes resulting from the 2014 Ziama and 2019 Jijel earthquakes (**a**), as well as the cumulative effect of the four main events of the Bejaia 2012–2013 sequence (**b**), displayed on optimally oriented fault planes. The figure has been modified based on the work of Yelles-Chaouche et al. (2021) and Boulahia et al. (2021) to include the area of the 2021 aftershock cluster

partitioned motion from along the thrust offshore system in eastern Algeria was transferred to the MAD fault; the transfer occurs by slip on the NW–SE right-lateral transverse fault system connecting the two previous systems

(Boulahia et al. 2021; Bendjama 2022; Abacha et al. 2023). The swarm-like seismic activity associated with hydrothermal sources along the NE-SW Jebel Safia Fault, east LKB, reveals the role played by fluids in triggering earthquakes

(Abacha 2015). The critical gap remaining is in Annaba on the offshore thrust faults, described from swath bathymetry and high-resolution seismic data (Kherroubi et al. 2009), which have not experienced significant earthquake activity, low or strong, for a long period of time, therefore, are the thrust faults locked or creeping aseismically? It is vital to identify stress release or building on these fault systems, similar to the gap on the thrust faults offshore GKB.

Conclusion

The mainshock and aftershocks of the 2021–2022 Bejaia Bay seismic sequence are an episode of the seismic crisis, which started in the Bejaia region since 2012. It shows the activation of an E-W thrust fault ramp in the margin toe of the Lesser Kabylia Block, which is composed of a main distinct fault labeled TF1, gently south-dipping, and belonging to a set of blind thrust faults. The active faults evidence the underthrusting below the Algerian margin, which might reflect the incipient stage of subduction. The seismic sequence aftershocks originate from coseismic stress transfer at a short distance from the mainshock. The tectonic loading is driven by Africa–Eurasia convergence. This new event gave the opportunity to detail the complex active deformation pattern in the Bejaia bay where a set of four main active faults converge. The current study shows the en echelon thrust fault system, which is dissected by strike-slip faults and may play a critical role in the rupture of concurrent segments. This study paves the way for future research, which should address the seismic gap on the activated area's eastern end and the GKB offshore system.

Declarations

References

Abacha I, Boulahia O, Yelles-Chaouche A, Semmane F, Beldjoudi H, Bendjama H (2019) The 2010 beni-Ilmane, Algeria, earthquake sequence: statistical analysis, source parameters, and scaling relationships. J Seismol 23:181–193. https://doi.org/10.1007/s10950-018-9800-7

Abacha I, Boulahia O, Yelles-Chaouche A et al (2023) The 24 January 2020 Mw 5.0 El Aouana Earthquake, Northeastern Algeria: insights into a new NW–SE right-lateral Bejaia–Babors shear zone. Pure Appl Geophys. https://doi.org/10.1007/s00024-023-03265-3

Abacha I (2015) Etude de la sismicité de la région Nord-Est de l'Algérie. Dissertation, University of Ferhat Abbas Sétif. http://dspace.univ-setif.dz:8888/jspui/handle/123456789/1802

Aidi C, Beslier MO, Yelles-Chaouche AK et al (2018) Deep structure of the continental margin and basin off Greater Kabylia, Algeria—new insights from wide-angle seismic data modeling and multichannel seismic interpretation. Tectonophysics. https://doi.org/10.1016/j.tecto.2018.01.007

Akoğlu AM, Jónsson S, Wang T et al (2018) Evidence for tear faulting from new constraints of the 23 october 2011 Mw 7.1 Van, Turkey, earthquake based on InSAR, GPS, coastal uplift, and field observations. Bull Seismol Soc Am. https://doi.org/10.1785/0120170314

Angelier J, Mechler P (1977) Sur une methode graphique de recherche des contraintes principales egalement utilisables en tectonique et en seismologie: la methode des diedres droits. Bull Soc Géol France. https://doi.org/10.2113/gssgfbull.S7-XIX.6.1309

Arab M, Rabineau M, Déverchère J et al (2016) Tectonostratigraphic evolution of the eastern Algerian margin and basin from seismic data and onshore-offshore correlation. Mar Pet Geol. https://doi.org/10.1016/j.marpetgeo.2016.08.021

Archuleta RJ, Cranswick E, Mueller C, Spudich P (1982) Source parameters of the 1980 Mammoth Lakes, California, earthquake sequence. J Geophys Res. https://doi.org/10.1029/JB087iB06p0459

Auzende JM, Bonnin J, Olivet JL (1975) La marge nord-africaine considérée comme marge active. Bull Soc Géol France. https://doi.org/10.2113/gssgfbull.S7-XVII.4.486

Benaouali-Mebarek N, Frizon de Lamotte D, Roca E et al (2006) Postcretaceous kinematics of the atlas and tell systems in central Algeria: early foreland folding and subduction-related deformation. Compt Rend Geosci. https://doi.org/10.1016/j.crte.2005.11.005

Bendjama H, Yelles-Chaouche A, Boulahia O et al (2021) The march 2017 earthquake sequence along the E-W trending McidAïcha-Debbagh fault, northeast Algeria. Geosci J 25:697–713. https://doi.org/10.1007/s12303-020-0059-y

Bendjama H (2022) Caractérisation des séquences sismiques récentes dans la région tectonique de la faille décrochante de Mcid Aïcha-Debbagh, Nord-Est de l'Algérie. Dissertation, University of Abou Bekr Belkaid Tlemcen. http://dspace.univ-tlemcen.dz/handle/112/19802

Boudiaf MA (1996) Etude sismotectonique de la région d'Alger et de la Kabylie (Algérie). Dissertation, University of Montpellier.

Bougrine A, Yelles-Chaouche AK, Calais E (2019) Active deformation in Algeria from continuous GPS measurements. Geophys J Int. https://doi.org/10.1093/gji/ggz035

Bouillin JP (1986) Le "bassin maghrebin"; une ancienne limite entre l'Europe et l'Afrique a l'ouest des Alpes. Bull Soc Géol France 2(4):547–558

Boulahia O, Abacha I, Yelles-Chaouche A et al (2021) Recent seismic activity in the Bejaia–Babors region (Northeastern Algeria): the case of the 2012–2013 Bejaia Earthquake Sequences. Pure Appl Geophys 178(1253):1279. https://doi.org/10.1007/s00024-021-02711-4

Brune JN (1970) Tectonic stress and the spectra of seismic shear waves from earthquakes. J Geophys Res 75:4997–5009

Chatelain J (1978) Étude fine de la sismicité en zone de collision continentale à l'aide d'un réseau de stations portables : la région

Hindu–Kush–Pamir. Dissertation, University of Paul Sabatier Toulouse

Delvaux D (2012) Release of program Win-Tensor 4.0 for tectonic stress inversion: Statistical expression of stress parameters, EGU General Assembly, Vienna, 2012. Geophysical Research Abstracts, 14, EGU2012–EGU5899.

Déverchère J, Yelles K, Domzig A, Mercier de Lépinay B et al (2005) Active thrust faulting offshore Boumerdes, Algeria, and its relations to the 2003 Mw 6.9 earthquake. Geophys Res Lett. https://doi.org/10.1029/2004GL021646

Domzig A (2006) Déformation active et récente, et structuration tectonosédimentaire de la marge sous-marine algérienne. Dissertation. University of Western Brittany Brest.

Duarte JC, Rosas FM, Terrinha P et al (2013) Are subduction zones invading the Atlantic? Evidence from the southwest Iberia margin. Geology. https://doi.org/10.1130/G34100.1

Efron B (1982) The Jackknife, the Bootstrap and Other Resampling Plans. CBMS-NSF Regional Conference Series in Applied Mathematics, Monograph 38, SIAM, Philadelphia

Gutenberg B, Richter CF (1944) Frequency of earthquakes in California. Bull Seismol Soc Am 34:185–188

Hainzl S, Kraft T, Wassermann J, Igel H, Schmedes E (2006) Evidence for rainfall-triggered earthquake activity. Geophys Res Lett. https://doi.org/10.1029/2006GL027642

Hamai L, Petit C, Abtout A, Yelles-Chaouche A, Déverchère J (2015) Flexural behaviour of the north Algerian margin and tectonic implications. Geophys J Int. https://doi.org/10.1093/gji/ggv098

Hamai L, Petit C, Le Pourhiet L et al (2018) Towards subduction inception along the inverted North African margin of Algeria? Insights from thermo-mechanical models. Earth Planet Sci Let. https://doi.org/10.1016/j.epsl.2018.08.028

Hanks TC, Wyss M (1972) The use of body-wave spectra in the determination of seismic-source parameters. Bull Seismol Soc Am. https://doi.org/10.1785/BSSA0620020561

Haskov J, Ottemöller L (1999) SEISAN earthquake analysis software. Seismol Res Let. https://doi.org/10.1785/gssrl.70.5.532

Jolivet L, Faccenna C (2000) Mediterranean extension and the Africa-Eurasia collision. Tectonics. https://doi.org/10.1029/2000TC900018

Kherroubi A, Déverchère J, Abdelkarim Y et al (2009) Recent and active deformation pattern off the easternmost Algerian margin, Western Mediterranean Sea: new evidence for contractional tectonic reactivation. Marine Geol. https://doi.org/10.1016/j.margeo.2008.05.016

Kissling E (1994) Initial reference model in local earthquake tomography. J Geophys Res 99:19635–19646

Klein F (2002) User's guide to HYPOINVERSE-2000, a Fortran program to solve for earthquake locations and magnitudes, USGS Open-File Report 02–171, vers. 1, p 123

Klingelhoefer F, Déverchère J, Graindorge D et al (2022) Formation, segmentation and deep crustal structure variations along the Algerian margin from the SPIRAL seismic experiment. J Afri Earth Sci. https://doi.org/10.1016/j.jafrearsci.2021.104433

Leffondré P, Déverchère J, Medaouri M (2021) Ongoing inversion of a passive margin: spatial variability of strain markers along the Algerian margin and basin (Mediterranean Sea) and seismotectonic Implications. Front Earth Sci. https://doi.org/10.3389/feart.2021.674584

Lin J, Stein RS, Meghraoui M, Toda S, Ayadi A, Dorbath C, Belabbes S (2011) Stress transfer among en echelon and opposing thrusts and tear faults: triggering caused by the 2003 Mw = 6.9 Zemmouri, Algeria, earthquake. J Geophys Res. https://doi.org/10.1029/2010JB007654

Magistrale H, Day S (1999) 3D simulations of multi-segment thrust fault rupture. Geophys Res Lett. https://doi.org/10.1029/1999GL900401

Meghraoui M, Pondrelli S (2012) Active faulting and transpression tectonics along the plate boundary in North Africa. Ann Geophys. https://doi.org/10.4401/ag-4970

Meghraoui M, Cisternas A, Philip H (1986) Seismotectonics of the lower cheliff basin: structural background of the El Asnam (Algeria) earthquake. Tectonics. https://doi.org/10.1029/TC005i006p00809

Mesimeri M, Karakostas V, Papadimitriou E, Tsaklidis G, Jacobs K (2018) Relocation of recent seismicity and seismotectonic properties in the Gulf of Corinth (Greece). Geophys J Int 212:1123–1142. https://doi.org/10.1093/gji/ggx450

Mihoubi A, Schnürle P, Benaissa Z et al (2014) Seismic imaging of the eastern Algerian margin off Jijel: integrating wide-angle seismic modeling and multichannel seismic pre-stack depth migration. Geophys J Int 198:1486–1503. https://doi.org/10.1093/gji/ggu179

Mock S, Herwegh M (2017) Tectonics of the central Swiss Molasse Basin: Post-Miocene transition to incipient thick-skinned tectonics? Tectonics. https://doi.org/10.1002/2017TC004584

Rivera L, Cisternas A (1990) Stress tensor and fault plane solutions for a population of earthquakes. Bull Seismol Soc Am. https://doi.org/10.1785/BSSA0800030600

Schettino A, Turco E (2006) Plate kinematics of the western Mediterranean region during the Oligocene and early Miocene. Geophys J Int. https://doi.org/10.1111/j.1365-246X.2006.02997.x

Schorlemmer D, Wiemer S, Wyss M (2005) Variations in earthquake-size distribution across different stress regimes. Nature. https://doi.org/10.1038/nature04094

Spakman W, Wortel MJR (2004) A tomographic view on western mediterranean geodynamics. In: Cavazza W, Roure F, Spakman W, Stampfli GM, Ziegler P (eds) THE TRANSMED Atlas, The Mediterranean Region from Crust to Mantle (Springer, Berlin, pp. 31–52). https://doi.org/10.1007/978-3-642-18919-7_2

Stein R (1999) The role of stress transfer in earthquake occurrence. Nature. https://doi.org/10.1038/45144

Strzerzynski P, Déverchère J, Cattaneo A, Domzig A, Yelles-Chaouche AK (2010) Tectonic inheritance and Pliocene-Pleistocene inversion of the Algerian margin around Algiers: insights from multibeam and seismic reflection data. Tectonics. https://doi.org/10.1029/2009TC002547

Thomas WA (1990) Controls on locations of transverse zones in thrust belts. Eclogae Geol Helv 83(3):727–744

Trugman DT, Shearer PM (2017) GrowClust: a hierarchical clustering algorithm for relative earthquake relocation, with application to the Spanish springs and Sheldon, Nevada, earthquake sequences. Seismol Res Lett 88:379–391. https://doi.org/10.1785/0220160188

Utsu T, Ogata Y et al (1995) The centenary of the Omori formula for a decay law of aftershock activity. J Phys Earth 43(1):1–33. https://doi.org/10.4294/jpe1952.43.1

Van Hinsbergen DJJ, Vissers RLM, Spakman W (2014) Origin and consequences of western Mediterranean subduction, rollback, and slab segmentation. Tectonics. https://doi.org/10.1002/2013TC003349

Wada I, Wang K (2009) Common depth of slab-mantle decoupling: reconciling diversity and uniformity of subduction zones. Geochem Geophys Geosyst. https://doi.org/10.1029/2009GC002570

Waldhauser F, Ellsworth WL (2000) A double-difference earthquake location algorithm: Method and application to the northern Hayward fault. Bull Seismol Soc Am 90:1353–1368

Waldhauser F (2001) HypoDD a program to compute double-difference hypocenter locations, U.S. Geological Survey Open File report, 01–113

Yagi Y, Nishimura N (2011) Moment tensor inversion of near-source seismograms. Bull Inter Inst Seismol Earthquake Eng 45:133–138

Yelles K, Lammali K, Mahasas A, Calais E, Briole P (2004) Coseismic deformation of the May 21 st, 2003, Mw = 6.8 Boumerdes

earthquake, Algeria, from GPS measurements. Geophys Res Let. https://doi.org/10.1029/2004GL019884

Yelles-Chaouche A, Roger J, Déverchere J et al (2009) The 1856 Tsunami of Djidjelli (Eastern Algeria): seismotectonics modelling and hazard implications for the Algerian coast. Pure Appl Geophys. https://doi.org/10.1007/978-3-0346-0064-4_14

Yelles-Chaouche AK, Abacha I, Boulahia O et al (2021) The 13 July 2019 Mw: 5.0 Jijel earthquake, northern Algeria: an indicator of active deformation along the eastern Algerian margin. J of Afr Earth Sci. https://doi.org/10.1016/j.jafrearsci.2021.104149

Yelles-Chaouche A, Aidi C, Beldjoudi H et al (2022) The recent seismicity of northern Algeria: the 2006–2020 catalogue. Med Geosc Rev. https://doi.org/10.1007/s42990-022-00092-x

Yelles-Chaouche AK, the Maradja Team (2006) A Morphotectonic overview of the deforming seaward boundary of the Africa-Europe convergence zone off Algeria from Oran to Annaba. EGU Vienna

Yelles-Chaouche AK, the Spiral Team (2010) From Maradja to Spiral surveys. Recent and active deformation of the Algerian margin and the evidence of contractionnal reactivation. ESC Montpellier

Yukutake Y, Yoshihisa I (2017) Why do aftershocks occur? Relationship between mainshock rupture and aftershock sequence based on highly resolved hypocenter and focal mechanism distributions. Earth Planets Space. https://doi.org/10.1186/s40623-017-0650-2

Zanchi A, D'Adda P, Zanchetta S et al (2012) Syn-thrust deformation across a transverse zone: the Grem-Vedra fault system (central Southern Alps, N Italy). Swiss J Geosci. https://doi.org/10.1007/s00015-011-0089-6